

# **LABEL-FREE PARTICLE SORTING: TECHNOLOGY AND BIOLOGICAL APPLICATIONS**

**LICENTIATE**

**Kushagr Punyani**



**LUND**  
UNIVERSITY

Division of Solid State Physics, and NanoLund

Department of Physics, Lund University,

Lund, Sweden.

March 14, 2018

ISBN Print 978-91-7753-620-8

ISBN Electronic 978-91-7753-621-5

No speck too small...



# CONTENTS

Contents	i
Abstract	iii
Acknowledgements	v
List of Figures	ix
Chapter 1 Introduction	1
<b>1.1</b> Conventional Particle Sorting	3
<b>1.2</b> Label-Free Microfluidic Particle Sorting	5
Chapter 2 Microfluidic Sedimentation	9
<b>2.1</b> Background	9
<b>2.2</b> Results and Discussion	14
<b>2.3</b> Conclusions	17
<b>2.4</b> Methods	18
Chapter 3 Sorting by Deterministic Lateral Displacement	21
<b>3.1</b> Background	21
<b>3.2</b> Results and Discussion	24
<b>3.3</b> Conclusions	27
<b>3.4</b> Methods	27
Chapter 4 Effect of Post Shapes in DLD	31
<b>4.1</b> Background	31
<b>4.2</b> Results and Discussion	32

<b>4.3 Future Work</b>	36
<b>4.4 Methods</b>	37
<b>Chapter 5 Towards Sorting of Bio-responsive Hydrogel Particles</b>	39
<b>5.1 Background</b>	39
<b>5.2 Results and Discussions</b>	49
<b>5.3 Future Work</b>	53
<b>5.4 Methods</b>	54
<b>Bibliography</b>	57

## ABSTRACT

While centrifugation and membrane filtration are arguably the most common techniques of cell sorting or fractionation in life sciences, they are not suitably customized for a variety of biological samples and applications. The current licentiate thesis is concerned with microfluidic label-free technologies of particle sorting, designed and applied to specific applications in biology. It aims to develop and adapt particle sorting technologies for enrichment and purification of a variety of cells, facilitating analysis and diagnosis. We suggest and demonstrate the principle and working of a microfluidic sedimentor, fractionating cell samples based on mass density and particle size by exploiting the concept of terminal velocity in a microfluidic channel. Its utility has been demonstrated by separating red blood cells and *Trypanosoma* parasites, which are responsible for causing the tropical neglected disease of sleeping sickness. Next, the work delves into the technique of Deterministic Lateral Displacement (DLD), applying the method to separate another tropical parasite, causing Leishmaniasis, from red blood cells. Further, the effect of post architecture in DLD has been investigated by altering post shapes, with the aim of determining predictable design principles in DLD devices with L-shaped posts. Finally, we propose sorting of cancer cells encapsulated in microbeads composed of extra-cellular matrix, using DLD, in order to study the interaction of the cells with their microenvironment, and subsequent remodeling of the extra-cellular matrix.



## ACKNOWLEDGEMENTS

In the summer of 2014, right after completing my undergraduate thesis, I visited Lund for the first time, for the interview of this doctoral position. The fifteen minutes presentation of my undergraduate research projects turned into an hour long discussion. I met several of my future colleagues and collaborators at the First Workshop of the EU project LAPASO, which was soon to christen me RT-1. The scientific objectives of the project and the fluid conversation made me immediately realize that this was the place to be. The week vaulted in a scholarly rapture, full of enthusiastic discussions and project plans. For the entire experience (still going), I am greatly thankful to Jonas Tegenfeldt. His constant support, drive, patience and belief in me have kept this journey going. The academic guidance I have received from him has helped me realize this thesis and the encompassed research.

I would also like to thank Jason Beech for his crucial scientific input and constructive critique, as well his enthusiasm and motivation. His technical knack and microscopy skills have been greatly helpful in the laboratory. My sincere thanks also goes to Stefan Holm for taking responsibility of my general training in laboratory, and his help in lithography, electron microscopy and optical microscopy. Interesting Discussions

I would like to acknowledge Clément Regnault and Mike Barrett at the Wellcome Trust Centre for Molecular Parasitology, University of Glasgow, United Kingdom thanks to whom the work in Chapter 3 has been realized. I am also greatly thankful to Laura Ciufredda and Lisa Ranford-Cartwright at the University of Glasgow, for the open scientific dialogue and collaboration, also involving Oskar Ström and Stefan Holm. Further the team of Gerhard Gompper at Forschungszentrum Jülich, Germany, including Zunmin Zhang, Ewan Henry and Dmitry Fedosov has greatly contributed to the foundation of the work in Chapter 4

with their exhaustive simulations and scientific cooperation. I would also like to thank our collaborators at Technische Universität Dresden (BIOTEC), Germany, including Salvatore Girardo, Jochen Guck, Ahmad Ahsan Nawaz, Katrin Wagner, Nicole Traeber and Heike Neumann for hosting me, and the training and experiments in droplet microfluidics, RT-DC and AFM, included in Chapter 5. Collaboration and extensive discussions with Chris Madsen and Alberto García Mariscal at Cancer and Matrix Remodeling, Division of Translational Cancer Research, Lund University have also helped shape the work proposed in Chapter 5. Also, I would like to acknowledge Monica Brivio at Micronit, Enschede, The Netherlands for our discussions for microfluidic device fabrication and sourcing. And finally, thanks to Gerda Rentschler for all the administrative help during the LAPASO travels, meetings, workshops and project-reports.

For the scientific discussions and intellectual input to various projects in this journey, I am also extremely thankful to Emma Sparr, Feifei Peng, Linda Månsson, Peter Jönsson and Peter Schurtenberger at Physical Chemistry, Lund University; Kristina Persson at the Division of Clinical Chemistry and Pharmacology, Lund University; Henric Bergman and Ricky Ansell at Swedish National Forensic Centre, Linköping; Alison Dun (Heriot-Watt University, Edinburgh, United Kingdom) and the alumni and participants of Edinburgh Super Resolution Imaging Consortium Summer School 2015.

The open and collaborative dialogue in the framework of LAPASO provided for personal and professional growth. I would like to thank all the fellows, partners and associate-partners of LAPASO, for their efforts to realize a highly functional and concerted training network. Further, members of Jonas' group, including Alexandra Kühnlein, Bao Dang Ho, Elke Hebisch, Jason Beech, Karl Adolfsson, Oskar Ström, Rebekah Kim, Si Hoai Trung Tran, Stefan Holm, Stefano Scaramuzza, have greatly contributed by helping to create a conducive scientific and social environment in the group. The affiliation of Biogroup at FTF has

provided a cooperative platform for researchers with similar interests to hold scientific communication. For the candid discussions and the invaluable cooperation in the labs, I would like to thank Anders Kyrstig, Cassandra Niman, Christelle Prinz, Damiano Verardo, Frida Lindbergh, Heiner Linke, Inga von Ahnen, Laura Abariute, Martin Hjört, Mercy Lard and Zhen Li.

Further, the open, enthusiastic and pioneering environment of NanoLund, and the division of Solid State Physics has been bliss to work in. I would like to thank the administrative, managerial and technical staff that leaves no stone unturned to contribute and create this atmosphere. I would like to include a special note of thanks for Abdul-Rehman Hakim, Charlotte Solberg, Eva Lenhoff, Louise Baldetorp, Margareta Forsberg and Mia Hedin for all their administrative help; Maria Messing for organizing the scientific outreach programs; Anneli Löfgren, Dan Hessman and Line Lundfald for their continuous efforts striving for improvements in the working environment; Anders Kvennefors, Bengt Mueller, Dmitry Suyatin, George Rydnemalm, Håkan Lapovski, Ivan Maximov, Maria Huffman, Mariusz Graczyk and Sara Ataran for their help for the unceasing improvement and maintenance the Lund Nano Lab; Johanna Mosgeller and Janne Mårtensson for taking care of the IT-infrastructure of the entire division (and solving my problems). I would also like to thank Jonas Johansson and Anneli Löfgren for their invaluable mentorship and guidance during this PhD.

The importance of the entire support system that has kept my back during this journey – my family and friends, cannot be undermined. I would like to thank Giulio, Sunil, Anita, Luna, Regina, Artis, Damiano, Ali, Shishir, Vishal, Lipakshi, Akshita, Priyanka and Pranav. They have been the brakes in my bike and checkpoints in mitosis.

XOXO



## LIST OF FIGURES

<b>Figure 1.1</b> Vincent van Gogh’s ‘Man with Winnow’ (September 1881, left) and ‘Woman Churning Butter’ (October 1881, right) (1, 2).	1
<b>Figure 1.2</b> Schematic illustrations of various conventional parting sorting methodologies.	4
<b>Figure 1.3</b> Schematic illustrations of some key examples of label-free passive microfluidic sorting.	6
<b>Figure 2.1</b> Schematic illustration of the principle of the microfluidic sedimentor.	11
<b>Figure 2.2</b> Displacement of a polystyrene microsphere with $RP = 5 \mu m$ and $\rho P = 1.04 g.cm^{-3}$ , undergoing creaming in a straight channel in fluid of $\rho F = 1.59 g.cm^{-3}$ and $\eta F = 1.5 mPa.s$ .	14
<b>Figure 2.3</b> a) Separation of PS (purple) and PMMA (green) particles in the microfluidic sedimentor setup at 4 mbar operating pressure. Scale bar 100 $\mu m$ . b) Outlet distributions of the PMMA and PS particles, measured orthogonal to the flow direction at operating pressures of 4 mbar (left) and 6 mbar (right).	15
<b>Figure 2.4</b> Separation of <i>T. cyclops</i> trypomastigotes from erythrocytes in microfluidic sedimentor. Scale bar 50 $\mu m$ .	16
<b>Figure 2.5</b> Microscopy setup for observations in microfluidic sedimentor. The sample stage can be translated vertically and to pan along the length of the device, as well be rotated to align the microfluidic channels horizontally.	19
<b>Figure 3.1</b> Schematic illustration of the principle of Deterministic Lateral Displacement.	22
<b>Figure 3.2</b> Diagrams illustrating morphology of a) an erythrocyte and b) an <i>L. mexicana</i> promastigote.	24

- Figure 3.3** Outlet distributions of erythrocytes (RBCs) and *L. mexicana* promastigotes in the 13 section DLD device, at incremental operational pressures (a – h). The Outlet Regions plotted on the abscissa correspond to different sections along the length of the device. 25
- Figure 4.1** SEM image of PDMS stamp of the DLD array (scale bar: 25  $\mu\text{m}$ ), with enlarged schematic of device parameters ( $G = 10 \mu\text{m}$ ;  $P = 15 \mu\text{m}$ ;  $R_L = 12.5 \mu\text{m}$ ;  $\lambda = 25 \mu\text{m}$ ;  $0.4 \mu\text{m} < \pm\Delta\lambda < 8.0 \mu\text{m}$ ). 32
- Figure 4.2** a) Fluid flow profiles in arrays with L-shaped posts, obtained from DPD simulations. b) Predicted sorting behavior of different sized particles in arrays of different row shift fractions,  $\varepsilon = \Delta\lambda/\lambda$ . 33
- Figure 4.3** Observed sorting dynamics in DLD arrays with L-shaped posts. 34
- Figure 4.4** Zig-zag events in sections with a) positive and b) negative row shifts. Trajectories of particles of normalized diameter 0.49, across  $\sim 2$  periods, in an array with periodicity of 20.8, with row shift fractions c)  $\varepsilon = + 0.05$  and d)  $\varepsilon = - 0.05$ . 35
- Figure 4.5** Mixed modes in trajectories of particles of normalized diameter 0.49, across 10 periods in an array with  $\varepsilon = 0.15$  and periodicity of 6.25. Scale bar 100  $\mu\text{m}$ . 36
- Figure 5.1** Schematics illustrating 2D and 3D cell culturing techniques. 40
- Figure 5.2** The interplay of extra-cellular matrix and cancer development. Graphics reproduced from reference (99) by permissions under Creative Commons Attribution License (CC BY). 44
- Figure 5.3** Common methods of passive droplet generation. a) Co-flow, b) Cross-flow, and c) Focused-flow droplet generators. Reused from reference (103) with permission from the Royal Society of Chemistry. 48

**Figure 5.4** Generation of 11  $\mu\text{m}$  polyacrylamide microbeads in a focused-flow device at 10X magnification (scale bar 50  $\mu\text{m}$ ). Inset shows a zoomed in image at the point of generation (scale bar 25  $\mu\text{m}$ ). Average diameter of droplets was measured to be  $12.7 \pm 0.9 \mu\text{m}$ . Dispersed phase is polyacrylamide monomer solution, while continuous phase is HFE-7500 with a custom-synthesized fluorosurfactant. 49

**Figure 5.5** Young's modulus of the polyacrylamide beads, measured using Atomic Force Microscopy (AFM) and Real Time Deformability Cytometry (RT-DC). 50

**Figure 5.6** Time evolution of collagen-1 droplets in a flow-focused droplet device. On the left, droplet generation rate and diameters of the collagen droplets at 0 and 20 minutes. On the right, micrographs showing drastic reduction in droplet generation rate; flow is left to right (scale bar 100  $\mu\text{m}$ ). 51

**Figure 5.7** Effect of operational pressure on the droplet diameter and generation rate in Dev75. On the right, micrographs at 10X magnification showing droplet generation at corresponding operating pressures; flow is left to right. Scale bar 200  $\mu\text{m}$ . 52

**Figure 5.8** Collagen-1 droplets in Dev75 with continuous phase (Picosurf-1 (2% in FC-40)) and dispersed phase (collagen-1 pre-polymer solution) at 26 mbar and 25 mbar, and b) 38 mbar and 24 mbar. The highlighted area shows gelation of collagen-1 in the device due to local heating from illumination. 53

**Figure 5.9** Setup for Collagen-1 droplet generation. The sample reservoirs are connected to a pressure pump, and can be immersed in ice to prevent gelation of Collagen-1. 55



## Chapter 1 INTRODUCTION

The Early works of Vincent van Gogh – the famous Dutch painter, revolve around the ‘Peasant Genre,’ showcasing the life and struggles of the peasants. Interestingly, the recurrent agricultural activities depicted in some of his works (see Figure 1.1) are reminiscent of the fundamental element of this thesis – particle sorting, albeit in a primitive and arguably rudimentary form. The two illustrated activities in Van Gogh’s works below, winnowing and churning, essentially, are particle separation methods that employ external forces to sort particles of different size and density. It would be beyond the interests of this thesis to discuss the historical evolution of these, and other such methods, but of great significance to mention their gravity and influence on development of filtration and centrifugation procedures that form the backbone of several products and technologies in modern society.

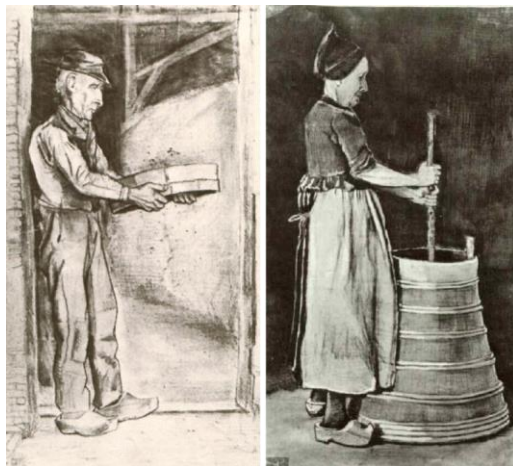


**Figure 1.1** Vincent van Gogh’s ‘Man with Winnow’ (September 1881, left) and ‘Woman Churning Butter’ (October 1881, right) (1, 2).

Wide use of particle filtration and centrifugation in agricultural and other consumer-oriented manufacturing procedures paved the way for use and

adaptation of these technologies in laboratory analytics and healthcare. The twentieth century also witnessed inter-dependent, yet great technological developments in *in vitro* cell culturing, production and purification of biologicals, and other lab analytical techniques. These techniques included gel electrophoresis (3), radioimmunoassays (4), enzyme linked immunoassays (ELISA) (5, 6), blotting techniques (7-9) and nucleic acid amplification (10). At this point, I take the liberty of streamlining the discussion and jetting into the late twentieth century's quest for miniaturization. With a variety of laboratory analytical techniques and their complements available, came the critical analysis and improvement of the said technologies. A unique school of thought emerged, fueled by miniaturization of fabrication - characteristic of microelectromechanical systems (MEMS), and focused on performing these analyses at low sample volume flux. The real thrust came from the development of the *bio-suitable* rapid prototyping microfabrication technique, called soft lithography (11). This gave birth to an intellectual flood of controlled engineering of microfluidic systems, and design of biomedical microelectromechanical systems (bioMEMS), synonymous with lab-on-a-chip (LOC) and micro total analysis systems ( $\mu$ TAS).

The applications of these systems are diverse, and form a spectrum from sample preparation to sensing to creating precisely controlled microenvironments, or combinations thereof. In a matter of speaking, we hop on to this train of bioMEMS to further improve and understand the particle sorting technologies currently in use, and under research and development, elaborated on in Sections 1.1 and 1.2, respectively. The contribution of this work in the field will be discussed in the subsequent chapters. In brief, the current work explores and exploits the sorting techniques of Microfluidic Sedimentation and Deterministic Lateral Displacement, which will be explained in Chapter 2 and Chapter 3, respectively.

## 1.1 CONVENTIONAL PARTICLE SORTING

Progress in life science research and the healthcare industry has been closely linked to the available technologies. The current section will give a brief discussion of technologies currently widely used in life science laboratories dealing with particle or cell separation.

Fundamentally, one of the simplest, yet rigorous techniques, **membrane filtration** exploits use of a thin semi-permeable material that leads to separation of components of the sample upon application of an external force. Essentially, the method relies on the ability of the particles to penetrate through the orifices in a porous substrate (see Figure 1.2). Membrane filtration is widely used in water filtration, as well as separation of cells or particles of different sizes. Essentially, membrane filtration is size based sorting, and has also been adapted as a sterilization method for aseptic technique in cell culturing. Despite their wide use and success, membrane filters are highly prone to clogging, and not amenable to post-fabrication operational modifications. They are best suited for small volume batch-filtration processes, especially when dealing with cells.

Arguably, the most widely used fractionation technique, **centrifugation** exploits the differences in sedimentation velocities of particles in a given carrier fluid, to temporally or spatially fractionate the sample in a closed volume. Essentially, the sedimentation of the particles is accelerated by application of a centrifugal force. Sample volumes ranging from a few hundred microliters to several hundred milliliters can be sorted in typical lab centrifuges or ultracentrifuges. In its most common form, a batch process, centrifugation can be used in several modes, based on the sample properties and the attenuation of the carrier/base fluid.

**Gel electrophoresis** is another class of widely used particle sorting technique that exploits differential electrophoretic mobility of particles in an electric field (see Figure 1.2). The electrophoretic mobility of a particle is a function of its net

charge and mass. This is commonly used for separation of Nucleic acids and polypeptide molecules of different molecular masses in agarose gels or denaturing polyacrylamide gels, respectively. Protein molecules can also be sorted in a non-denaturing polyacrylamide gel for different electrophoretic mobility. Further, gel electrophoresis can also be used with a pH-gradient coupled gel, to migrate particles – proteins or even cells – based on their isoelectric points, for sorting or analytical purposes.

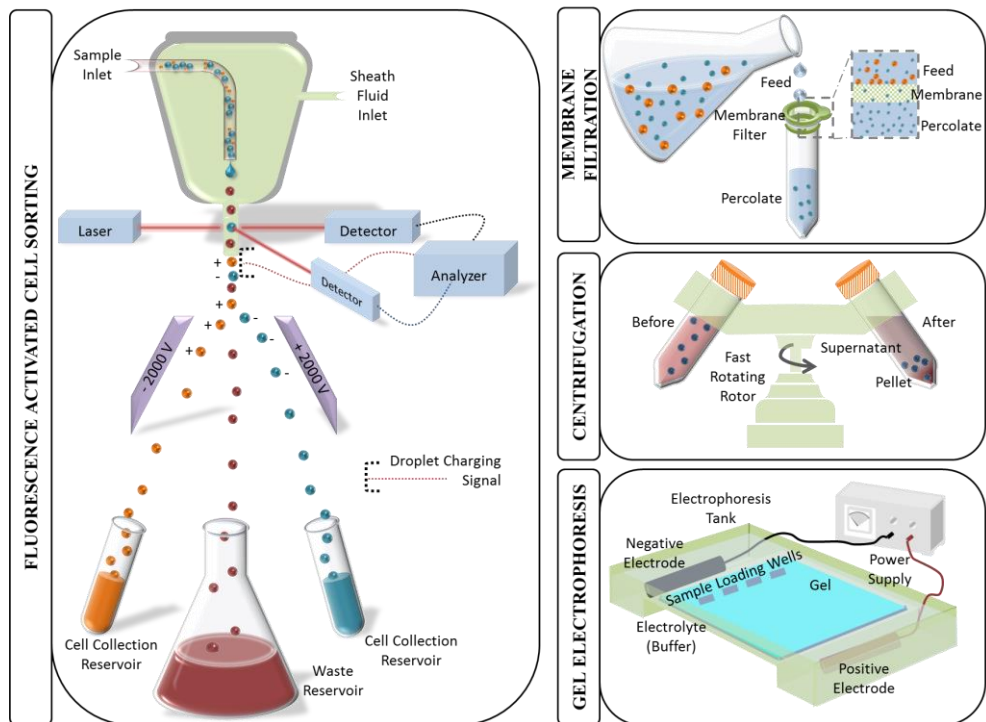


**Figure 1.2** Schematic illustrations of various conventional parting sorting methodologies.

The sorting techniques discussed above exploit physical characteristics of particles, while being predominantly unaffected by their biochemical function. However, to sort cells based on their functional properties, conventional cell sorting techniques call for the use of probes and labels. **Fluorescence Activated**

**Cell Sorting** (FACS) (see Figure 1.2) and **Magnetic Activated Cell Sorting** (MACS) are two such widely used techniques that exploit surface markers on the cells for differential labelling with antibodies coupled to fluorophores or magnetic beads, respectively. The distinct advantage is that these techniques open doors for functional sorting of cells, however they are limited by the sensitivity and specificity of biomarkers and antibodies, need of active particle deflectors, high operational and reagent cost, and the bulky apparatus. These factors have undoubtedly impeded the use of FACS and MACS in resource-poor or mobile settings.

It is clear that the conventional particle sorting has several technological impediments when it comes to continuous operation. These methods are difficult to track on the fly, and the sorting efficiencies can only be estimated indirectly. Most often, sorting is based on average particle size, and particle shape – although important – cannot be exploited. Biophysical characteristics such as mass density and particle deformability are often convoluted with particle size, or may even be inaccessible. While FACS and MACS introduce a functional component to otherwise morphology based fractionation, the techniques are futile if appropriate surface markers for the desired biochemical signature to be studied are unavailable. At this point, the discussion shall enter the realm of microfluidics, and the doors it opens in the field of particle sorting.

## **1.2 LABEL-FREE MICROFLUIDIC PARTICLE SORTING**

As discussed in the previous section, conventional particle sorting techniques are batch processes, and do not provide means to sort cells based on their morphology in a label-free manner. This section briefly introduces various microfluidic particle sorting techniques with the advantage of label-free and continuous operation. Broadly, label-free microfluidic particle sorting methods can be categorized as passive or active techniques, or a combination thereof (12). While passive sorting

techniques employ hydrodynamic forces and barriers to sort particles, active sorting methods may be actuated by magnetic, optical, acoustic or electrokinetic forces. These methods are suited for particles inherently different in their physical characteristics, or can also employ a combination of probes and labels.

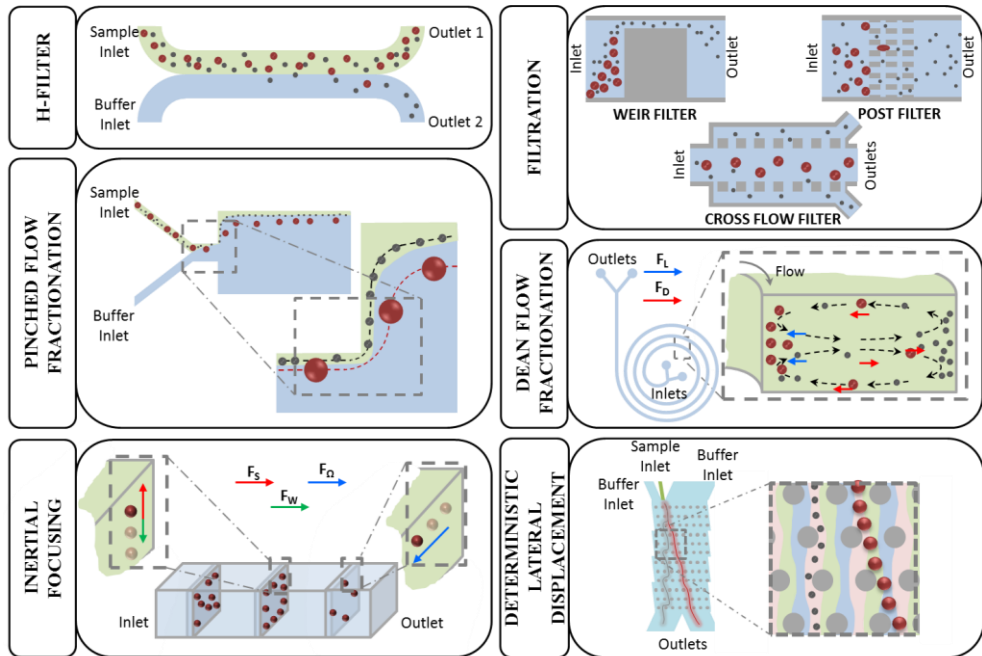


**Figure 1.3** Schematic illustrations of some key examples of label-free passive microfluidic sorting.

H-filters, Pinched Flow Fractionation, Inertial and Dean Flow Fractionation, Filtration and Hydrodynamic Filtration, and Deterministic Lateral Displacement are some key examples of passive cell sorting techniques, illustrated in Figure 1.3.

**H-filters and T-sensors** are purely based on the interplay between convective flow and particle diffusion (13, 14) or motility (15), and are suitable for selectively enriching particles with higher diffusion coefficients or active motility. **Pinched flow fractionation** employs constriction in a microfluidic channel and the size-dependent alignment of the particles to the side-wall (16, 17). The technique has

also been extended to couple the effect of gravitational and centrifugal forces (18). **Inertial and Dean flow fractionations** exploit the counteracting shear gradient-induced lift force and wall-effect-induced lift force (19, 20). **Filtration** spatially restricts or prevents particles above a critical diameter to flow through a microfilter. Several designs of filters exist, including Weir filters, pillar filters, and cross flow filters (21). **Hydrodynamic Filtration**, on the other hand, uses the virtual width of the side channel stream, regulated by its flow rate, wherein the smaller particles are allowed to flow out to the side channels, while the stream in the main channel gets enriched for large particles (22). **Deterministic Lateral Displacement** (DLD) comprises a large post array, wherein each row of posts has been slightly shifted with respect to the previous one (23). The consequent streamline pattern is a characteristic of the device architecture, and can hence be exploited to separate particles based on their size.

In general, all these sorting techniques have the advantages of being continuous, label-free, portable, and amenable to operational modifications and flexibility. Chapter 2 describes a novel label-free microfluidic sorting approach to separate particles based on their sedimentation velocities, and fractionation of the simian sleeping sickness parasite *Trypanosoma cyclops* from erythrocytes. Further, the current work exploits DLD to a great extent, and hence it has been explained in further detail in Chapter 3, where DLD has been employed to sort the human cutaneous leishmaniasis parasite, *Leishmania mexicana* from erythrocytes. Chapter 4 presents a systematic study on the effect of an alternative cross section of the posts in DLD, and the consequent design and sorting advantages.

At this junction, it is interesting to mention that the discussed hydrodynamic forces that govern various label-free passive microfluidic particle sorting techniques, including DLD, work through a dialogue between the particles being sorted, the carrier fluid and the channel geometry. This facilitates the exploitation of multiple biophysical characteristics of a cell that may be inaccessible through conventional

particle sorting techniques. These characteristics, essentially the viscoelastic properties of the particles, open a new realm of probing into the cell, without relying on the availability of surface markers. Such modes of sorting have previously been exploited by some groups – to fractionate leukocytes from whole blood by deformability in microfluidic ratchet cell sorting (24); to separate differentially stiffened subpopulations of erythrocytes using DLD (25); to sort elastic microcapsules using obstacle mediated constriction at high shear rates (26); to separate cell lines of neuroblastoma and adult epithelial cancer origins from blood by deformability coupled filtration (27); and to sort DAPI-stained *Plasmodium falciparum* infected erythrocytes from healthy erythrocytes by margination (28). Chapter 5 lays the foundation for a novel approach to sort cancer cells based on metastatic potential using a combined approach of using droplet microfluidics and DLD.

## Chapter 2 MICROFLUIDIC SEDIMENTATION

### 2.1 BACKGROUND

**A**round 1870, the Swiss biologist Friedrich Miescher first reported isolation of nuclein, now better known as deoxyribonucleic acid (DNA), from leucocytes (29). Besides the seminal discovery, his constant struggle of obtaining pure leucocytes from pus-laden bandages led him to use sedimentation to get pure cells from pus – which later came to be known as unit-gravity sedimentation. By the end of the decade, the Swedish engineer Carl Gustaf Patrik de Laval had introduced the first centrifugal cream separator (30). Thereafter, it took around fifty years for the first ultracentrifuge to be adapted for laboratory use, invented and improved by the Swedish chemist Theodor Svedberg (31). Since then, the centrifuge has become commonplace in every chemistry and biology laboratory.

The method has been adapted to sedimenting colloids, cells and synthetic particles of various sizes and densities. In its simplest form, differential centrifugation is a temporal particle sorting method, and is best suited for harvesting all the particles denser than the medium. When used with continuous or step density gradients, it can be used to achieve temporal or spatial separation of the particles, depending on the differences in the density of the particles and the gradient. However, the versatility of the technique has conventionally hit a roadblock when it comes to getting rid of the bulky apparatus, performing continuous particle separation or processing sample volumes lower than a few hundred microliters. Significant work has been done to exploit the principles of the hearty centrifuge on lab-on-a-disk platforms, while rescuing the short-lived compact disks from becoming obsolete. Most of the lab-on-a-disk work centers around technology development for controlled actuation of fluid flow (32). However, little effort has gone into translating the sedimentation rate dictated particle fractionation on these platforms,

albeit some groups have adapted differential or density gradient centrifugation (33-35) and blood separations (36, 37) on the disk, and hematocrit measurements (38). Despite this progress, the work has not been translated widely. A recent review article on centrifugal microfluidics briefs the various technologies required to realize the method (39). In essence, the requirement of valves, spinning platforms, operationally and economically expensive optics for observing the rotating channels have impeded the use of centrifugal microfluidics.

In essence, centrifugation trumps sedimentation by facilitating enormous accelerations, however, several applications exploiting centrifugation do not need the typical g-values used, and can also lead to sample damage due to high shear forces. Little work has been done to perform density or sedimentation rate based separations on lab-on-a-chip systems. In 2005, Benincasa *et al.* demonstrated a microfluidic setup for unit-gravity sedimentation with bifurcated inlet and outlet, to separate two different cell types, primarily by size (40). In 2007, Huh *et al.* reported a device with a widening channel, wherein the particles were first focused parallel to the gravitational force, followed by positional separation orthogonal to the gravitational force, and finally the separation was amplified leading to separation (41). This work, however, was also limited to separation based on size and not density of the particles. In 2014, Sugiyama *et al.* presented a sedimentation based separation device using a straight channel and a bifurcation at the outlet wherein they showed separation of model particles of close densities (42). However, the work was restricted to separation of particles of similar size only. In 2014, Son *et al.* reported a sedimentation and filtration based plasma extraction from blood (43). Further, Holm *et al.* reported a two-tiered density-coupled DLD device for bimodal size-independent separation of particles based on density (44). Recently, Maria *et al.* also demonstrated a plasma separation device based on sedimentation and wettability gradient (45). The principle of these works is very simple, but not suitable for a variety of samples.

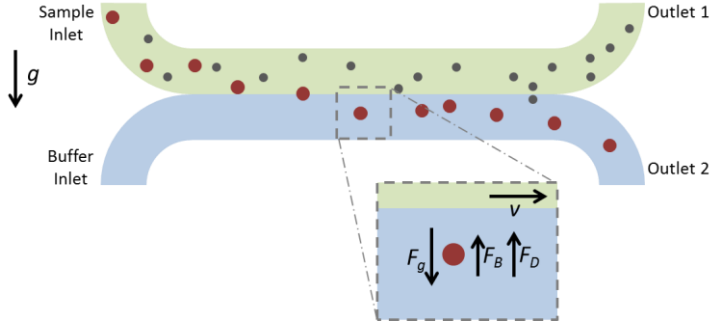


**Figure 2.1** Schematic illustration of the principle of the microfluidic sedimentor.

In this chapter, we report a simple device exploiting separation based on sedimentation of particles along the flow in a straight channel. The inlet and outlet are bifurcated and identical, and the design is as described in Figure 2.1. Essentially, the device can be used for versatile operation and different samples, by altering the fluid flows. It is essential at this point to discuss the physical principle of sedimentation that acts upon the particles in the device to effectuate separation.

## THEORY

In Figure 2.1, the convective fluid flow is illustrated left to right with a velocity,  $v$ . Also, there exists a gravitational force acting on the particle,  $F_g$  described by equations 2.1 and 2.2, where  $m_p$ ,  $\rho_p$  and  $R_p$  are the mass, density and radius of the particle, and  $\rho_F$  and  $\eta_F$  are the density and viscosity of the fluid, respectively. Although most biological particles of interest are irregular in shape, for simplicity, the particles in this discussion are assumed to be spheres. The subsequent error is expected to be minor.

$$F_g = m_p g \quad 2.1$$

$$F_g = \frac{4}{3} \pi R_p^3 \rho_p g \quad 2.2$$

For most biological samples, the particles are denser than the carrier fluid, hence, as the particle sediments with instantaneous velocity  $v_S$ , a buoyant force  $F_B$  and a drag force  $F_D$  act on the particle, thereby counteracting  $F_g$ .

$$F_B = \frac{4}{3}\pi R_p^3 \rho_F g \quad 2.3$$

$$F_D = 6\pi\eta_F R_p v_S \quad 2.4$$

Under steady state, the three forces are counterbalanced and equal, hence the particle does not undergo acceleration, but settles with a constant terminal velocity  $v_S = v_T$ .

$$v_T = \frac{2 R_p^2}{9 \eta_F} (\rho_p - \rho_F) g \quad 2.5$$

For sedimentation of distance  $x$  in a channel of length  $L$ , the linear velocity of the particle in the device can be estimated to:

$$v_L = \frac{2 R_p^2 L}{9 \eta_F x} (\rho_p - \rho_F) g \quad 2.6$$

However, before the steady state is achieved, as the particle begins to sediment, it accelerates with non-zero acceleration  $a$ , while the net force  $F$  acting on the particle, described in equation 2.7, approaches zero.

$$F = m_p a = F_g - F_B - F_D \quad 2.7$$

Substituting the terms from equations 2.2 – 2.4, it is possible to derive the acceleration  $a$ , where  $A = \frac{(\rho_p - \rho_F)g}{\rho_p}$  and  $B = \frac{9}{2} \frac{\eta_F}{\rho_p R_p^2}$  are constants for a given fluid-particle system.

$$a = \frac{(\rho_p - \rho_F)g}{\rho_p} - \frac{9}{2} \frac{\eta_F}{\rho_p R_p^2} v_S \quad 2.8$$

$$a = A - B v_S \quad 2.9$$

The time  $t_e$  required to achieve the velocity  $v_S$  can be described by:

$$t_e = \frac{v_S}{a} \quad 2.10$$

For steady state ( $v_S = v_T$ ), substituting the expression for  $v_T$  from equation 2.5, we find that an analytical solution for  $t_e$  is not possible (see equation 2.11). This reinforces the assumption of  $\lim t_e \rightarrow \infty$ , only at which the theoretical sedimentation velocity reaches a numerical constant. Hence, it is of interest to obtain a time estimate at which the sedimentation velocity approaches terminal velocity.

$$a = \frac{(\rho_p - \rho_F)g}{\rho_p} - \frac{9}{2} \frac{\eta_F}{\rho_p R_P^2} \frac{2 R_P^2}{9 \eta_F} (\rho_p - \rho_F)g = 0 \quad 2.11$$

It is possible to select a time  $t_e$ , at which  $v_S$  is a fraction of  $v_T$ , where  $k_t \in (0,1)$ , as described in equation 2.12. Also, at time  $t_e$ , the acceleration  $a$  can be represented by equation 2.14.

$$v_S = k_t v_T \quad 2.12$$

$$a = \frac{v_S - 0}{t_e} = \frac{k_t v_T}{t_e} \quad 2.13$$

Substituting equations 2.12 and 2.13 in equation 2.10, we get:

$$t_e = \frac{k_t v_T}{A - kBv_T} = \frac{2}{9} \frac{k_t}{1 - k_t} \frac{R_P^2 \rho_p}{\eta_F} \quad 2.14$$

Also, from equation 2.14, one can derive the relationship between  $t_e$  and  $v_S$ .

$$t_e = \frac{v_S}{1 - k_t} \frac{\rho_p}{(\rho_p - \rho_F)g} \quad 2.15$$

For typical parametric values of a relevant particle-fluid system ( $R_P = 5 \mu m$ ,  $\rho_p = 1.1 g.cm^{-3}$  and  $\eta_F = 1 mPa.s$ ) the time taken by the particle to achieve a sedimentation velocity equivalent to 99.99% of the terminal velocity ( $v_T =$

$5.4 \mu\text{m} \cdot \text{s}^{-1}$ ) is estimated to be  $t_e = 0.6 \text{ ms}$ . Further, for extreme values of the said parameters ( $R_p = 50 \mu\text{m}$ ,  $\rho_p = 2.0 \text{ g} \cdot \text{cm}^{-3}$  and  $\eta_F = 1 \text{ mPa} \cdot \text{s}$ ),  $v_T = 5.4 \text{ mm} \cdot \text{s}^{-1}$  and  $t_e = 0.1 \text{ s}$ . Hence, it is safe to assume that the time to achieve steady state sedimentation can be neglected in our system

The following section reports our findings on sedimentation of synthetic and biological microparticles in the microfluidic sedimentor, described earlier. We demonstrate differential migration of synthetic microspheres based on density exploiting unit-gravity microfluidic sedimentation. Further, biological particles with known density differences have been used to establish a proof of principle at relevant scales for particle density and size. The experimental setup has been described in the following sections, and also shown in Figure 2.5.

## 2.2 RESULTS AND DISCUSSION

### SEDIMENTATION VELOCITY AND TIME TO STEADY STATE

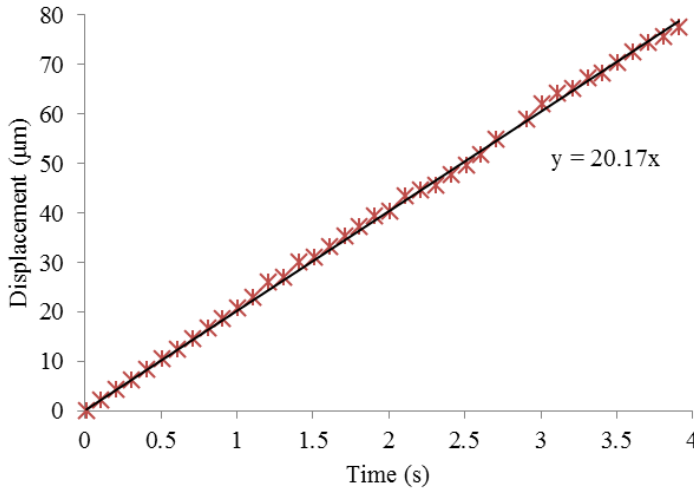


**Figure 2.2** Displacement of a polystyrene microsphere with  $R_p = 5 \mu\text{m}$  and  $\rho_p = 1.04 \text{ g} \cdot \text{cm}^{-3}$ , undergoing creaming in a straight channel in fluid of  $\rho_F = 1.59 \text{ g} \cdot \text{cm}^{-3}$  and  $\eta_F = 1.5 \text{ mPa} \cdot \text{s}$ .

In order to confirm that the particles do not undergo acceleration under relevant time scales and distances in the microfluidic sedimentor, polymeric microspheres of known size and density were introduced in a straight channel with a fluid of known density and viscosity. The system was perturbed by rotation vertically, and the particles undergoing sedimentation and creaming were immediately tracked. Figure 2.2 shows displacement of a polystyrene microsphere with  $R_p = 5 \mu\text{m}$  and  $\rho_p = 1.04 \text{ g.cm}^{-3}$ , undergoing creaming in a fluid with  $\rho_f = 1.59 \text{ g.cm}^{-3}$  and  $\eta_f = 1.5 \text{ mPa.s}$ . As evident, the vertical velocity of the particle,  $v_s$ , is constant; thereby proving that the time to reach equilibrium  $t_e$  is negligible. Further, the calculated terminal velocity of the particle  $v_T = 19.96 \mu\text{m.s}^{-1}$  matches with the experimentally observed value of  $20.17 \mu\text{m.s}^{-1}$ .

## SORTING OF POLYMERIC MICROSPHERES

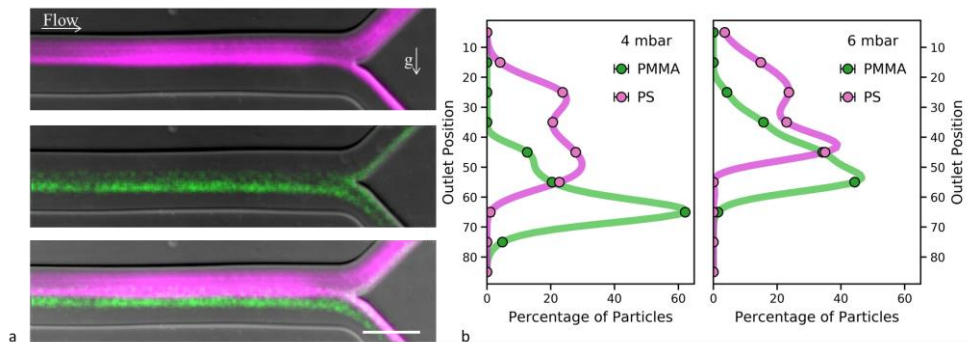


**Figure 2.3** a) Separation of PS (purple) and PMMA (green) particles in the microfluidic sedimentor setup at 4 mbar operating pressure. Scale bar  $100 \mu\text{m}$ . b) Outlet distributions of the PMMA and PS particles, measured orthogonal to the flow direction at operating pressures of 4 mbar (left) and 6 mbar (right).

Poly (methyl methacrylate) (PMMA) microspheres of diameter  $3.9 \mu\text{m}$  and density  $1.18 \text{ g cm}^{-3}$  were separated from polystyrene particles of diameter  $4.87 \mu\text{m}$  and density  $1.05 \text{ g cm}^{-3}$  in water, with a device of length  $1 \text{ cm}$  and width  $100 \mu\text{m}$  (see Figure 2.3 a). Although the PMMA particles were smaller, the sedimentation rates

of the particles were calculated to be  $0.167$  and  $0.073 \mu\text{m s}^{-1}$ , respectively, thereby demonstrating that the particle separation was a function of sedimentation rates, rather than the size.

The outlet distributions of the particles were also measured across the outlet (see Figure 2.3 b), at different flow speeds. As is evident from the two plots, the separation efficiency improves at slower flow rates. It was not possible to run controlled experiments at lower flow rates due to limitations of the flow setup.

### SEPARATION OF TRYPANOSOMES FROM ERYTHROCYTES

*Trypanosoma* is a genus of flagellated parasitic protozoans that are responsible for the disease sleeping sickness in humans, also known as Human African Trypanosomiasis (HAT). The parasite is transmitted to the human host by the bite of a carrier Tsetse fly, as metacyclic trypomastigotes. In the blood stream, they transform into trypomastigotes, spread to other fluid tissues and multiply. Trypomastigotes can invade the central nervous system through the blood brain barrier, leading to a number of neurological symptoms, including disruption of the sleep-wake cycle, and ultimately death.

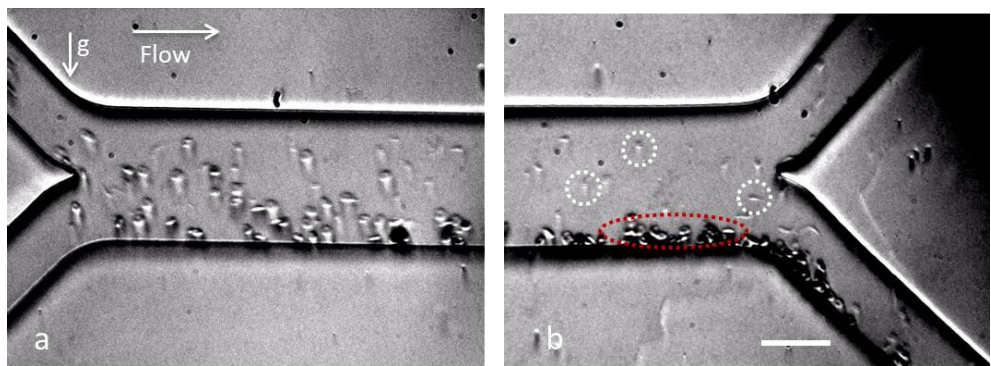


**Figure 2.4** Separation of *T. cyclops* trypomastigotes from erythrocytes in microfluidic sedimentor. Scale bar  $50 \mu\text{m}$ .

The standard diagnostic techniques include microscopic detection of the trypomastigotes in blood and lymph node aspirates. The diagnosis is difficult due to the abundance of erythrocytes in blood. Previous work has been done to isolate these parasites from blood using DLD (46). Here we show the possibility of separation of these parasites from erythrocytes using the microfluidic sedimentor (see Figure 2.4). The work uses model parasites of the species *T. cyclops* that are morphologically identical to the pathogenic species *T. brucei*.

The mass density of these parasites is not known, but an enrichment step for conventional diagnostics is buffy coat preparation via centrifugation, wherein the parasites end up as a part of the plasma. From literature, similar principles have been shown to be able to separate erythrocytes from plasma, but not particle fractionation for biological samples without the use of density gradients.

## 2.3 CONCLUSIONS

The current work describes a microfluidic sedimentor for fractionation of particles, based on mass density and terminal velocity. The principle of the technique has been validated by fractionation of polymeric microspheres of different density and sizes. The choice of particle parameters presented further substantiates the pivotal role of density of the particles in the sorting mechanism. Moreover, as a proof of principle, we demonstrate fractionation of a mixed sample of erythrocytes and *T. cyclops* trypomastigotes. Although, this separation is conventionally performed in a laboratory centrifuge, we show that the microfluidic sedimentor has the ability to readily perform diagnostically relevant separations. Further, the technique is easy to implement, highly versatile and with the potential to adapt to biological samples of interest. To the best of our knowledge, this is one of the first reports to fractionate particles using microfluidic differential sedimentation exploiting differences in density.

## 2.4 METHODS

### DEVICE FABRICATION

The devices were fabricated by replica molding in PDMS (Sylgard 184, Dow Corning, Midland, MI, USA). Briefly, the monomer and curing agents were thoroughly mixed in a ratio of 10:1, degassed in a vacuum desiccator for 20 minutes, followed by pouring over the device molds. The polymer was cured at 80°C for 60 minutes, following which the PDMS stamps were peeled off. The devices were cut out and holes were punched using biopsy punches. The PDMS stamps were then bonded to glass slides after oxygen plasma treatment at full power with 8 mbar oxygen for 30 s in Plasma Preen II-862 (Plasmatic Systems Inc., North Brunswick, NJ, USA). 10 µL of 0.2% aqueous solution of PLL(20)-g[3.5]-PEG(2) (SuSoS AG, Dübendorf, Switzerland) was immediately introduced in each of the inlet holes. Silicon tubes (5 – 30 mm long) were glued to the PDMS devices using Elastocil A07 (Wacker Chemie AG, München, Germany), and allowed to cure for at least an hour in a humidified chamber.

### *T. CYCLOPS* CULTURING AND SAMPLE PREPARATION

*T. cyclops* trypomastigotes were cultured in non-vented flasks at 28°C in Cunningham medium supplemented with 20% fetal calf serum (FCS) and 1% penicillin/streptomycin solution. The parasites were passaged with a 1:20 dilution every 2 weeks. The log phase cells were harvested by centrifugation at 1000g for 1 minute, and resuspended at the desired concentration in autoMACS™ running buffer (Miltenyi Biotech, Auburn, CA).

### BLOOD EXTRACTION AND SAMPLE PREPARATION

Up to 100 µL of blood was extracted from healthy volunteers using Haemic Haemolance® (MedCore AB, Sweden), and immediately diluted with around 10 volumes of autoMACS™ running buffer. The erythrocytes were harvested by

centrifugation at 1000 g for 1 minute, and resuspended at the desired concentration in PBS or autoMACS™ running buffer. If required, *T. cyclops* sample was mixed in the desired ratio with the erythrocytes.

## EXPERIMENTAL SETUP

The samples and buffers were loaded in the silicone inlet reservoirs, and the inlets were connected to Fluigent MFCS. Fluigent MFCS was controlled through Maesflow software. An upright microscope was reassembled to be able to mount the device vertically on the stage (see Figure 2.5). The device was mounted on a custom stage, and aligned horizontally with the help of a load suspended at the end of a thread. The images were captured using a CCD camera (Andor Luca S), and using 10X objective lens (Nikon Plan Fluor 10X/0.30).

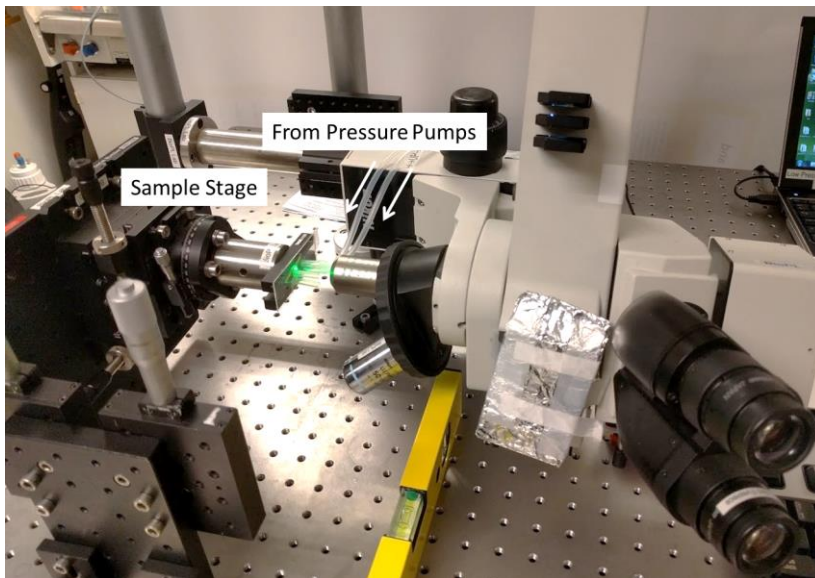


**Figure 2.5** Microscopy setup for observations in microfluidic sedimentor. The sample stage can be translated vertically and to pan along the length of the device, as well be rotated to align the microfluidic channels horizontally.



# Chapter 3 SORTING BY DETERMINISTIC LATERAL DISPLACEMENT

## 3.1 BACKGROUND

The previous chapter describes a simple and effective technique to translate unit-gravity sedimentation to microfluidic scale, while transforming the dimension of temporal separation to spatial fractionation. The sorting parameters of the microfluidic sedimentor, or a centrifuge for that matter, are a composite of the particle size and hydrodynamic shape, and the density difference between the particle and the carrier fluid. While it is possible to tune this density difference, the technique fails to deconvolve particle size, morphology and density. Most of the conventional and microfluidic particle sorting techniques discussed earlier, in Sections 1.1 and 1.2, do not address the problem of particle sorting by morphology. While size is the principle parameter governing separation in most techniques, there lacks a control over orientation and alignment of non-spherical particles.

The first to address this lacuna were Holm *et al.* in 2011, where they controlled the flow orientation of erythrocytes and *T. cyclops* in DLD by restricting the height of the channel, and demonstrated the separation of the two cell morphologies. This work also demonstrated the first method to access the diameter of the discocytes as a sorting parameter. Beech *et al.* further described the control over discocyte orientation in DLD in 2012 (25). In following years, other groups also demonstrated the potential of morphology based sorting in Hydrodynamic Filtration (47) and Inertial Focusing (48). However, these techniques do not exert the control over morphology based sorting at the level of device architecture, and particle migration is a convoluted function of particle size and morphology. On the other hand, in DLD, an anisotropic particle could be controlled to present two

different dimensions to the sorting array, and subsequently be sorted and fractionated based on the magnitude of the selected dimension. The following section describes the principle of DLD in greater detail.

### DETERMINISTIC LATERAL DISPLACEMENT

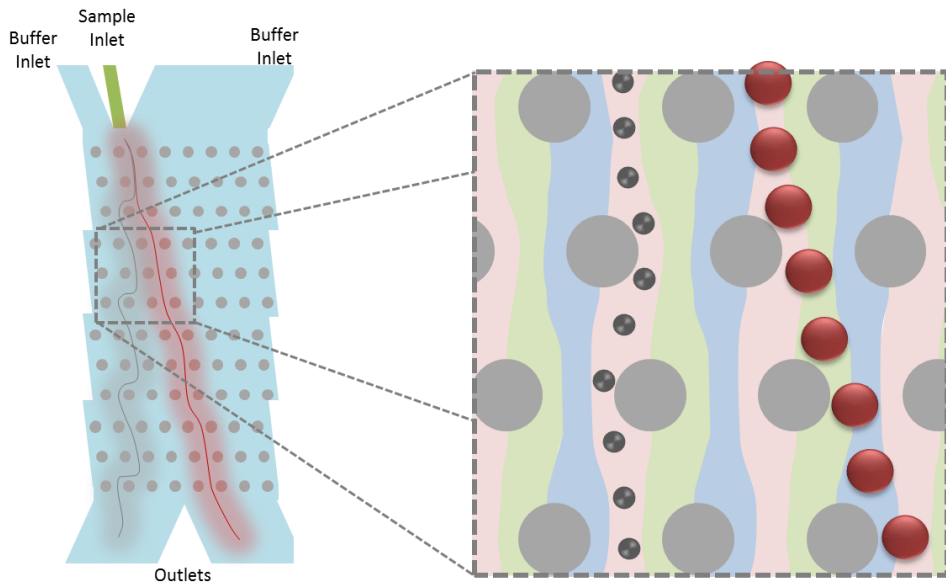


**Figure 3.1** Schematic illustration of the principle of Deterministic Lateral Displacement.

First described in 2004 by Huang *et al.* (23), DLD exploits a post array wherein each row is slightly shifted with respect to the one before, with a geometrical periodicity of  $N$ . A flow is applied perpendicular to the direction of the rows. As the dimensions of the channels are small, the flow is in laminar regime. The flow streamlines percolate through the array while meandering around the posts, while the array geometry determines the streamline configuration (see Figure 3.1). As every streamline circumnavigates every  $N$ th post in a column, the particles borne in the streamline may follow the flow and go around the post – zigzag event, or be bumped into the next streamline – displacement. This decision making depends on the array geometry, the resulting streamline pattern, and the

apparent particle size. The window of uncertainty in the choice of zigzag event versus displacement is very low, hence the name – Deterministic Lateral Displacement.

Owing to the complex geometry of a DLD array, it is difficult to predict the so-called critical diameter ( $D_c$ ) of the particle. In 2008, Davis empirically described  $D_c$  based on the array parameters – post diameter  $P$ , inter post separation  $G$  and row shift  $\Delta\lambda$  (49). This has facilitated the design of DLD devices for specialized applications.

$$D_c = 1.4G \frac{\Delta\lambda^{0.48}}{G + P} \quad 7$$

## LEISHMANIASIS

Leishmaniasis is a tropical parasitic disease, caused by the protozoa of the genus *Leishmania*, which is transmitted by infected sandflies of the genus *Phlebotomus* (50). Various *Leishmania spp.* are responsible for different leishmaniasis manifestations, namely cutaneous, mucocutaneous and visceral. While visceral leishmaniasis (VL) is the most serious, and potentially fatal, cutaneous leishmaniasis (CL) is the most common. CL is marked by lesions on the site of bite by the sandfly, and may also manifest as diffuse form with widespread skin lesions. Unfortunately, despite the high global burden of disease, CL fails to attract the attention of policymakers, due to low mortality rates; consequently, both treatment and diagnosis lag (51-53).

Diagnosis of leishmaniasis is performed by microscopic evaluation of the buffy coat from the blood or other aspirates. The evaluation is labor-intensive and difficult due to low parasitemia. Although, advanced techniques like PCR are available, they are economically unfeasible in the endemic areas. It is interesting to note that traditionally, *Leishmania spp.* are known to be obligate intracellular

parasites of the human host, present as sessile amastigotes in macrophages; and as extracellular flagellated promastigotes in the guts of phlebotomine sandflies (54). However, there is mounting evidence that CL promastigotes may be found in human blood as well (55). The current work exploits morphology based DLD to separate the CL parasite *L. mexicana* of the promastigote stage from erythrocytes as a proof of principle for a potential diagnostic applications.

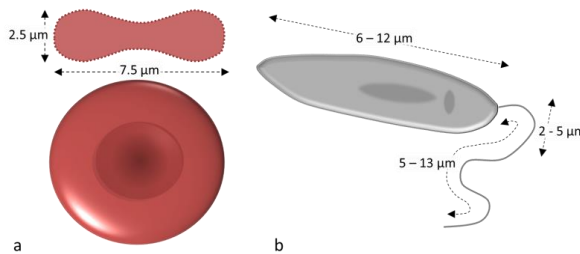


**Figure 3.2** Diagrams illustrating morphology of a) an erythrocyte and b) an *L. mexicana* promastigote.

## 3.2 RESULTS AND DISCUSSION

### SORTING OF *L. MEXICANA* PROMASTIGOTES FROM ERYTHROCYTES

A DLD device comprising of thirteen sections with different critical diameters in the range of 1 – 9 μm and inter-post gaps of 12 μm has been employed, identical to the one previously used by Holm *et al.* (46). The sorting is effectuated by the differences in shape and size of the two cell types. While erythrocytes are discoid shaped with a width of 2.5 μm and a diameter of 7.5 μm (46), *L. mexicana* promastigotes are flagellated and spindle shaped, with a width, cell body length and flagellum length of 2 – 5 μm, 6 – 12 μm and 5 – 13 μm, respectively (56) (see Figure 3.2).

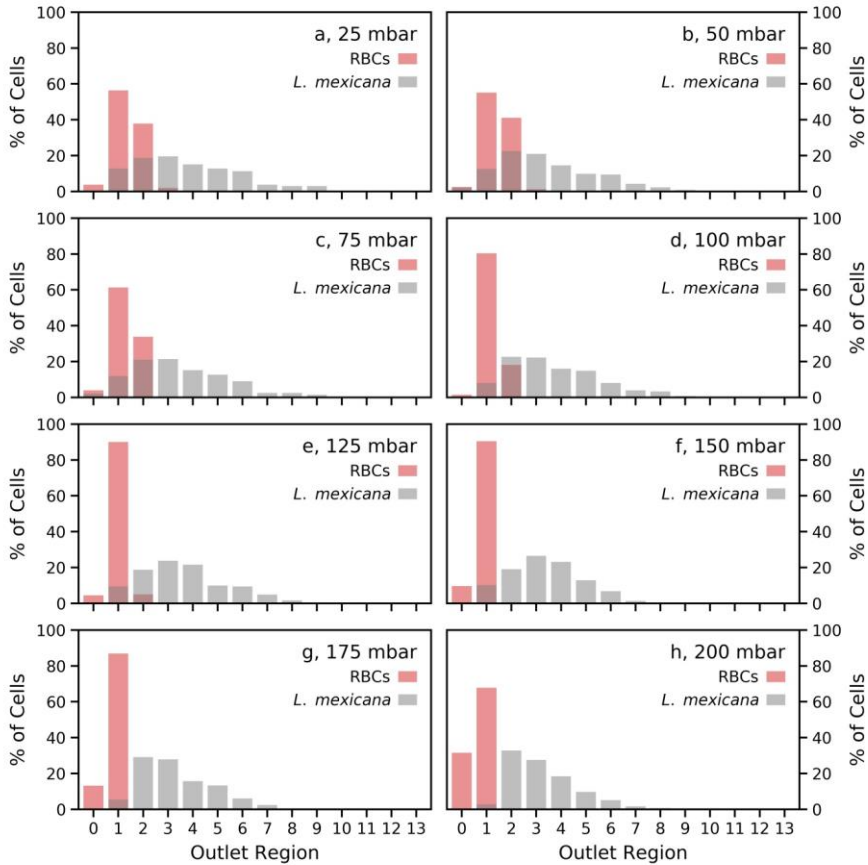


**Figure 3.3** Outlet distributions of erythrocytes (RBCs) and *L. mexicana* promastigotes in the 13 section DLD device, at incremental operational pressures (a – h). The Outlet Regions plotted on the abscissa correspond to different sections along the length of the device.

Driving the separation by erythrocyte diameter and the parasite width is almost obvious. However, it is important to consider the hydrodynamic behavior of erythrocytes under shear. Erythrocytes have previously been shown to considerably deform in DLD, even upon application of relatively low flow rates (25, 46). The DLD device was fabricated with a height of 8  $\mu\text{m}$  to primarily present the widths of the erythrocytes and promastigotes as sorting parameters.

Figure 3.3 summarizes the results of sorting a mixed sample of erythrocytes and *L. mexicana* promastigotes at different operational pressures (25 – 200 mbar). The outlet distributions of both cells types have been presented. Each outlet region corresponds to an interval of apparent size according to the critical diameters in the device sections (described in Table 1).

**Table 1** Outlet Positions in the DLD Device and Corresponding Apparent sizes

Outlet Region	Corresponding Apparent Size ( $\mu\text{m}$ )		Outlet Region	Corresponding Apparent Size ( $\mu\text{m}$ )	
	Minimum	Maximum		Minimum	Maximum
0	0	2.86	7	6.04	6.48
1	2.86	3.47	8	6.48	7.02
2	3.47	3.99	9	7.02	7.53
3	3.99	4.44	10	7.53	7.99
4	4.44	5.04	11	7.99	8.53
5	5.04	5.56	12	8.53	9.04
6	5.56	6.04	13	9.04	12.0

As evident in Figure 3.3 a – c, at low operational pressures, erythrocytes present an apparent diameter of up to 4  $\mu\text{m}$ . As the shear is low, the cells are free to rotate along the axis of flow direction. Also, the *L. mexicana* promastigotes show a wide distribution of apparent diameters of up to 7  $\mu\text{m}$ . As a result, the two distributions are poorly resolved with a significant overlap. As the pressure is increased further, increasing proportion of erythrocytes show a lower apparent size. This could owe to restriction of rotation along the axis of flow direction, or the increased shear rate and the resulting deformation of the erythrocytes. Consequently, the overlap in the outlet positions of the two cell types is reduced, despite the reduction in apparent size of the promastigotes (Figure 3.3 d – f). Also, the distribution of the promastigotes can be noted to shift to the right. This could be attributed to the increased rotation of the spindle shaped promastigotes against the posts,

perpendicular to the axis of flow direction, due to increased shear. Finally, the erythrocytes and the promastigotes are resolved at 200 mbar operating pressure (Figure 3.3 h).

### 3.3 CONCLUSIONS

The current chapter has exploited the principle of Deterministic Lateral Displacement to enrich promastigote stage of *L. mexicana* from erythrocytes. The fractionation has been performed using a DLD device that enables erythrocytes to present their morphological width to the flow, and be sorted by their widths. Consequently, a separation by width has been effectuated, thereby separating *L. mexicana* promastigotes from erythrocytes. To the best of our knowledge, this is one of the first reports to separate *L. mexicana* promastigotes from erythrocytes, and establishes a proof of principle for a diagnostic technique to enrich *L. mexicana* promastigotes in blood.

### 3.4 METHODS

#### DEVICE FABRICATION

The photomask for UV lithography were designed in L-Edit v.16.3 (Tanner Research, Monrovia, California, USA), and fabricated by DeltaMask (Enschede, The Netherlands). UV lithography was performed by the author and Stefan Holm, Lund University, with Karl Suss MJB4 (Munich Germany) on SU8 2000 (MicroChem, Newton, MA, USA) coated silicon wafers. SU8 processing and curing was carried out as per manufacturer's instructions. The silicon wafers were then surface passivated in a dehumidified environment at 175°C for 8 hours using Trichloro(1H,1H,2H,2H-perfluorooctyl)silane (Sigma-Aldrich Sweden AB).

The devices were fabricated by replica molding in PDMS (Sylgard 184, Dow Corning, Midland, MI, USA). Briefly, the monomer and curing agents were thoroughly mixed in a ratio of 10:1, degassed in a vacuum desiccator for 20

minutes, followed by pouring over the device molds. The polymer was cured at 80°C for 60 minutes, following which the PDMS stamps were peeled off. The devices were cut out and holes were punched using biopsy punches. The PDMS stamps were then bonded to glass slides after oxygen plasma treatment at full power with 8 mbar oxygen for 30 s in Plasma Preen II-862 (Plasmatic Systems Inc., North Brunswick, NJ, USA). 10 µL of 0.2% aqueous solution of PLL(20)-g[3.5]-PEG(2) (SuSoS AG, Dübendorf, Switzerland) was immediately introduced in each of the inlet holes. Silicon tubes (5 – 30 mm long) were glued to the PDMS devices using Elastocil A07 (Wacker Chemie AG, München, Germany), and allowed to cure for at least an hour in a humidified chamber.

#### *L. MEXICANA* CULTURING AND SAMPLE PREPARATION

*L. mexicana* promastigotes were cultured by Clément Regnault, University of Glasgow, in non-vented flasks at 25°C in HOMEM supplemented with 10% heat-inactivated fetal calf serum (FCS) and 1% penicillin/streptomycin solution. The parasites were passaged with a 1:20 dilution every 2 to 3 days. The log phase cells were harvested by centrifugation at 1000g for 10 minutes and resuspended at the desired concentration in autoMACS™ running buffer (Miltenyi Biotech, Auburn, CA).

#### BLOOD EXTRACTION AND SAMPLE PREPARATION

Up to 100 µL of blood was extracted from healthy volunteers using Haemedic Haemolance® (MedCore AB, Sweden), and immediately diluted with around 10 volumes of autoMACS™ running buffer. The erythrocytes were harvested by centrifugation and resuspended at the desired concentration in PBS or autoMACS™ running buffer.

#### EXPERIMENTAL SETUP

The samples and buffers were loaded in the silicone inlet reservoirs, and the inlets were connected to MFCS-4C Pressure controller (Fluigent, Paris, France). MFCS-

4C was controlled through Maesflow software (Fluigent, Paris, France). The experiments were performed under continuous observation on an inverted microscope. The images were captured using a CCD camera (Andor Luca S, Andor Technology, Belfast, Northern Ireland).



## Chapter 4 EFFECT OF POST SHAPES IN DLD

### 4.1 BACKGROUND

**D**LD was first reported by Huang *et al.* in 2004 (23) as a continuous size separation technique exploiting an array of circular posts. In 2006, Davis empirically described the critical diameter of the array based on the array parameters (see Equation 7) (49), and in 2009, Inglis *et al.* further improved the design of the array to compensate for irregular fluid flow at the edges (57). This facilitated prediction and robust design of DLD arrays for specific particle separation applications. Since then DLD has featured in several original scientific articles, demonstrating particle separation based on particle size, shape and deformability (25, 58). Also, in 2009, Louterback *et al.* reported the use of posts with right-angled triangular cross section, to introduce bi-directionality in the flow in the device, which the circular pillars could not impart (59). Soon afterwards, Louterback *et al.* published a thorough report on DLD arrays with equilateral triangular posts to benefit from reduced clogging and fluidic resistance (60). This was followed by adaptation of such triangular post arrays to separate various cell lines spiked in blood, by size, as a model for isolation of circulating tumor cells (61, 62). Alternative shapes including airfoils have been reported with specific applications for biological particles (63).

In 2011, Holm *et al.* reported the sporadic rotation of *T. cyclops* upon interaction with circular posts (46), followed by Beech *et al.* in 2012, to confine erythrocytes by device height, in order to access their diameters for sorting (25). This sparked an interest in accessing the hydrodynamic length of the anisotropic particles. Soon after, Zeming *et al.* demonstrated the use of I-shaped posts to enhance the particle rotation and access the morphological diameter of the discoid erythrocytes (64). More recently, Hyun *et al.* suggested topology optimized irregular post shapes suitable for minimizing clogging (65). With the exception of the latter, despite the

exploitation of technology, most of the previous work was based on inspection or speculation; no design principles were established for DLD arrays with alternative post shapes, until Zhang *et al.* in 2015 (66). Their work is largely *in silico* and of predictive nature. We teamed up with their group in 2016 to verify their predictions and further exploit alternative post shapes for particle separation in DLD. The current work describes our efforts to experimentally corroborate predicted results for L-shaped posts in DLD.

## 4.2 RESULTS AND DISCUSSION

### POST SHAPE AND DEVICE DESIGN

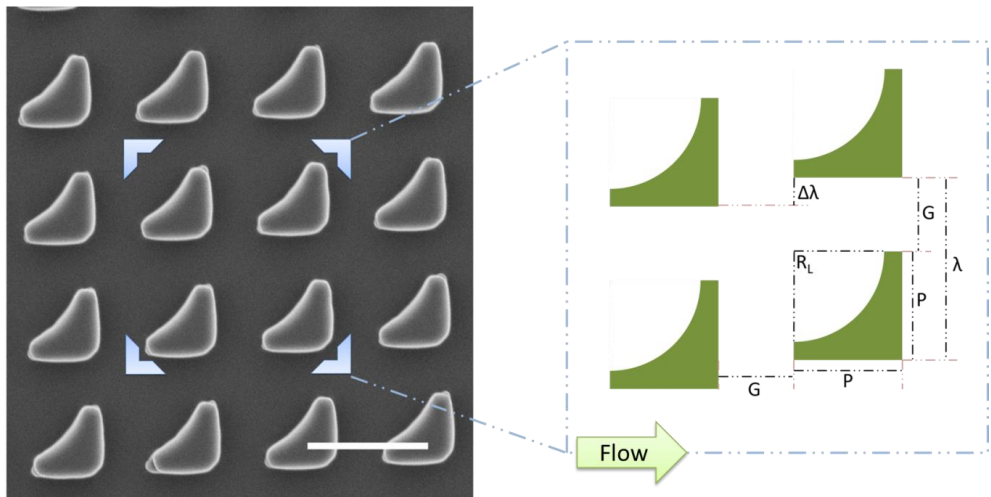


**Figure 4.1** SEM image of PDMS stamp of the DLD array (scale bar: 25  $\mu\text{m}$ ), with enlarged schematic of device parameters ( $G = 10 \mu\text{m}$ ;  $P = 15 \mu\text{m}$ ;  $R_L = 12.5 \mu\text{m}$ ;  $\lambda = 25 \mu\text{m}$ ;  $0.4 \mu\text{m} < \pm\Delta\lambda < 8.0 \mu\text{m}$ ).

Two DLD devices with a single inlet and outlet were designed, each with 9 consecutive sections, each with a separate critical diameter, in the range of  $0.4 \mu\text{m} < D_c < 8 \mu\text{m}$ . The devices were designed to facilitate long range analysis of particle behavior. Both the devices had L-shaped posts, as shown in Figure 4.1,

along with the device parameters. While all the sections in the first device have a positive row shift fraction, the second device comprised of negative row shifts. This, essentially, meant flipped posts with respect to the first device. Although in a circular or equilateral triangular post array, the two cases would be identical, here the asymmetry along the axis of flow direction introduces irregularity.

## SIMULATIONS

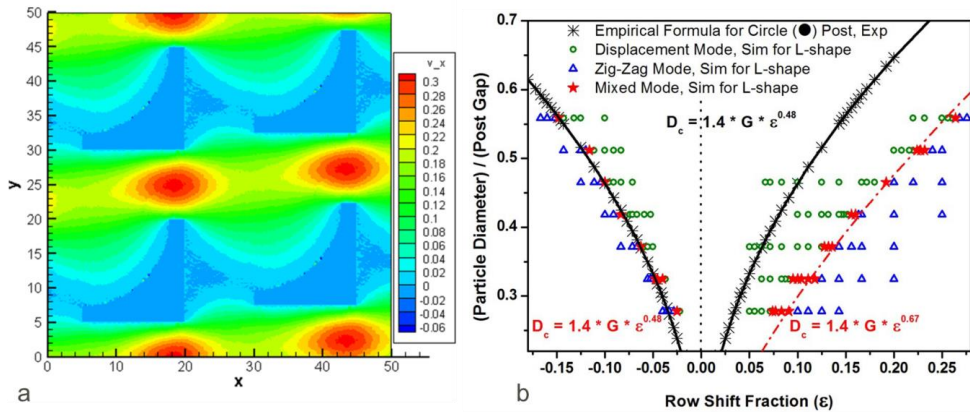


**Figure 4.2** a) Fluid flow profiles in arrays with L-shaped posts, obtained from DPD simulations. b) Predicted sorting behavior of different sized particles in arrays of different row shift fractions,  $\varepsilon = \Delta\lambda/\lambda$ .

Briefly, Dissipative Particle Dynamic (DPD) simulations were performed by Zunmin Zhang, similar to those described previously (66). The asymmetric fluid flow profiles in the L-shaped post arrays were as described in Figure 4.2a; red regions are characterized by high flow rates, while blue regions represent zero flow velocities. Also, Figure 4.2b shows the predicted behavior of particles of different diameters in DLD. It is interesting to note the difference in behavior of particles at negative versus positive row shifts, owing to the asymmetry of the post. Equations in red represent the predicted formulae for critical diameters in L-

shaped post arrays. The designs for experimental validation have been made with these parameters in mind.

## PARTICLE DYNAMICS IN DLD

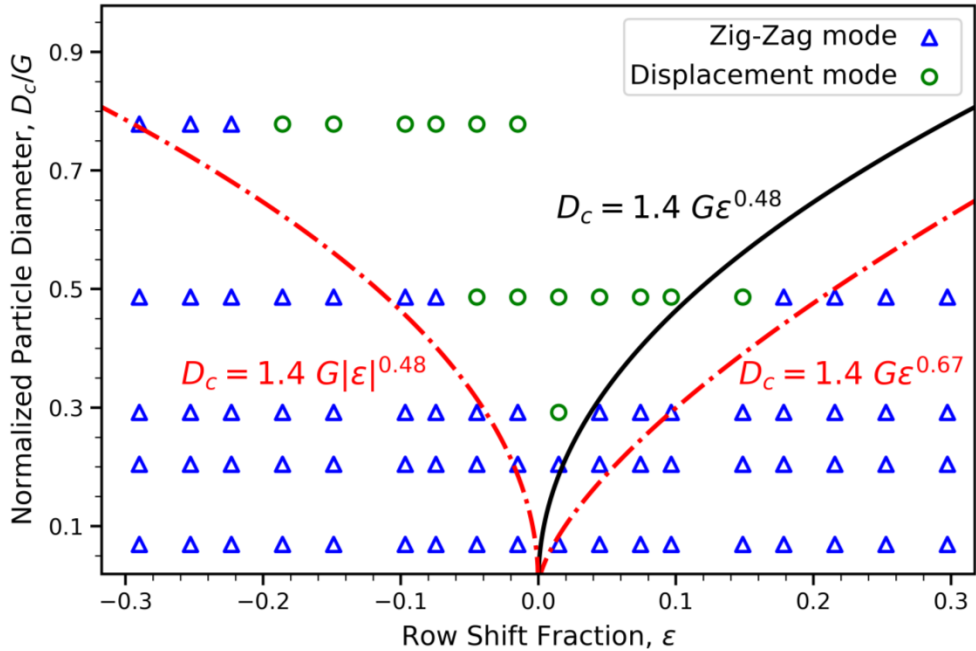


**Figure 4.3** Observed sorting dynamics in DLD arrays with L-shaped posts.

Particles of diameters between  $0.7 \mu\text{m}$  and  $7.7 \mu\text{m}$  were used to characterize the sorting modes in arrays with different row shift fractions in both the devices. Trajectories of the particles were analyzed for up to 10 periods to characterize the sorting modes. For sections with large periodicities, the particles were scanned over periods to characterize the sorting mode. For sections with small periodicities, several particles were observed over several periods at low magnifications. Figure 4.3 shows the sorting modes in periods of various row shifts. The experimental data is shown as scatter plot, with blue points representing the zig-zag mode, and green points representing the displacement mode. The equation and dashed line in black represent the expected critical

diameter loci in the plot for circular post arrays. The equations in red represent the predicted  $D_c$  in L-shaped post arrays. There is good agreement in the experimental and predicted results.

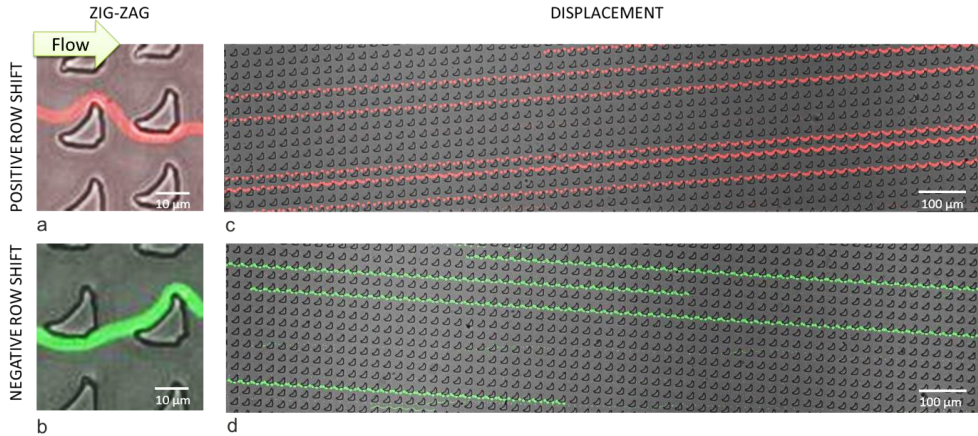


**Figure 4.4** Zig-zag events in sections with a) positive and b) negative row shifts. Trajectories of particles of normalized diameter 0.49, across  $\sim 2$  periods, in an array with periodicity of 20.8, with row shift fractions c)  $\varepsilon = +0.05$  and d)  $\varepsilon = -0.05$ .

Also, there is a visible difference in behavior of the particles at positive and negative row shifts. The asymmetry in the fluid flow around the posts in flow axis has also been substantiated by tracking particle trajectories at the zig-zag event and during displacement modes. Before the zig-zag event in positive row shift arrays, the particle sweeps along the concave face of the post, while in negative row shift arrays, it grazes at the convex face (see Figure 4.4 a, c). Also, in Figure 4.4 b and c, it is evident that the particle is in touch with different faces of the posts when under displacement. The two images have been taken with the same particle diameter in identical operation conditions in different sections with additive inverse row shifts.

The long-ranged data capture in our device helped us to capture the elusive mixed modes (see Figure 4.5). In 2011, Kulrattanarak *et al.* experimentally and

numerically analyzed mixed modes in DLD, besides the zig-zag and displacement modes (67). Essentially, particles undergoing mixed modes alternate between zig-zag and displacement modes, with a net non-zero migration angle. The presence of mixed modes is widely attributed to breakage of the flow symmetry in the unit cell.

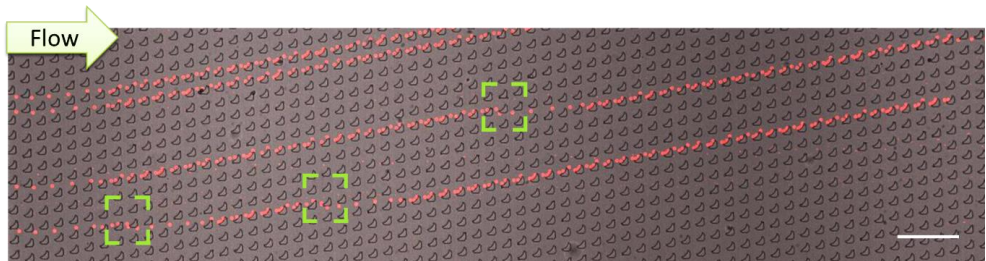


**Figure 4.5** Mixed modes in trajectories of particles of normalized diameter 0.49, across 10 periods in an array with  $\varepsilon = 0.15$  and periodicity of 6.25. Scale bar 100  $\mu\text{m}$ .

### 4.3 FUTURE WORK

The current experimental analysis of L-shaped post arrays has revealed interesting phenomena in particle behavior. The work would benefit from a detailed analysis of separation indices and trajectory tracking, and will be performed in the near future. The current fabricated devices are not ideal due to poor reproduction of the features, which further hampers quality and analysis of the data, as well as comparison with the simulations. We are working on fabrication of devices with better edge and vertex resolution. Further, it would be interesting to try sorting anisotropic particles in the L-shaped post arrays, and explore the contribution of particle rotation, if facilitated by the concave features in the posts.

## 4.4 METHODS

### DEVICE FABRICATION

The photomask for UV lithography were designed in L-Edit v.16.3 (Tanner Research, Monrovia, California, USA), and fabricated by DeltaMask (Enschede, The Netherlands). UV lithography was performed with Karl Suss MJB4 (Munich Germany) on SU8 2000 (MicroChem, Newton, MA, USA) coated silicon wafers. SU8 processing and curing was carried out as per manufacturer's instructions. The silicon wafers were then surface passivated in a dehumidified environment at 175°C for 8 hours using Trichloro(1H,1H,2H,2H-perfluorooctyl)silane (Sigma-Aldrich Sweden AB).

The devices were fabricated by replica molding in PDMS (Sylgard 184, Dow Corning, Midland, MI, USA). Briefly, the monomer and curing agents were thoroughly mixed in a ratio of 10:1, degassed in a vacuum desiccator for 20 minutes, followed by pouring over the device molds. The polymer was cured at 80°C for 60 minutes, following which the PDMS stamps were peeled off. The devices were cut out and holes were punched using biopsy punches. The PDMS stamps were then bonded to glass slides after oxygen plasma treatment at full power with 8 mbar oxygen for 30 s in Plasma Preen II-862 (Plasmatic Systems, Inc., North Brunswick, NJ, USA). Silicon tubes (5 – 30 mm long) were glued to the PDMS devices using Elastocil A07 (Wacker Chemie AG, München, Germany), and allowed to cure for at least an hour in a humidified chamber.

### EXPERIMENTAL SETUP

The samples and buffers were loaded in the silicon inlet reservoirs, and the inlets were connected to MFCS-4C Pressure controller (Fluigent, Paris, France). MFCS-4C was controlled through Maesflow software (Fluigent, Paris, France). The experiments were performed under continuous observation on Nikon Eclipse TE2000-U inverted microscope (Nikon Corporation, Tokyo, Japan). The images

were captured using an ultra-fast camera, Mikrotron Eosens Mini (Mikrotron GmbH, Germany) and various Nikon objective lenses (Plan Fluor 10X/0.30 and 4X/0.13).

# Chapter 5 TOWARDS SORTING OF BIO-RESPONSIVE HYDROGEL PARTICLES

## 5.1 BACKGROUND

In 1960, Wichterle and Lim wrote ‘Promising results have also been obtained in experiments in other cases, for example, in manufacturing contact lenses, arteries etc.’ (68). The letter published in *Nature* reported certain *plastics* or synthetic polymers with attributes that were ideal for use in specific applications *in vivo*. Over four years of their work had been dedicated to testing of poly(2-hydroxyethyl methacrylate) hydrogels as fillers after enucleation of the eye, besides the applications stated above. The choice of hydrogels over hard plastics for ocular fillers for Wichterle and Lim was based on the desirable mechanical characteristics, inertness to unfavorable bioprocesses, high water content, porosity for mass exchange and durability to biochemical wear and tear. These materials, coined hydrogels by Wichterle and Lim, were hydrophilic, three dimensional, crosslinked polymers, with water as the dispersed phase.

The definition of the term has stayed conserved over several decades, while the description has been found to include natural polymers as well. Since 1960s, synthetic, natural and hybrid hydrogels have found use in several biomedical fields including, but not limited to drug delivery (69), prosthesis (70), wound dressing (71), tissue culture (72, 73) and diagnostics (74). It is interesting to note that, originally, compared to the synthetic plastics, hydrogels were designed to be gentler on the cells and tissues in contact, which opened the doors for tissue engineering and 3D cell culturing. Today there is a wide consensus on the effort to mimic hydrogels as the extra-cellular matrix (ECM), with a significant effort invested in 3D cell culturing (75-78).

## ECM, HYDROGELS AND 3D CELL CULTURES

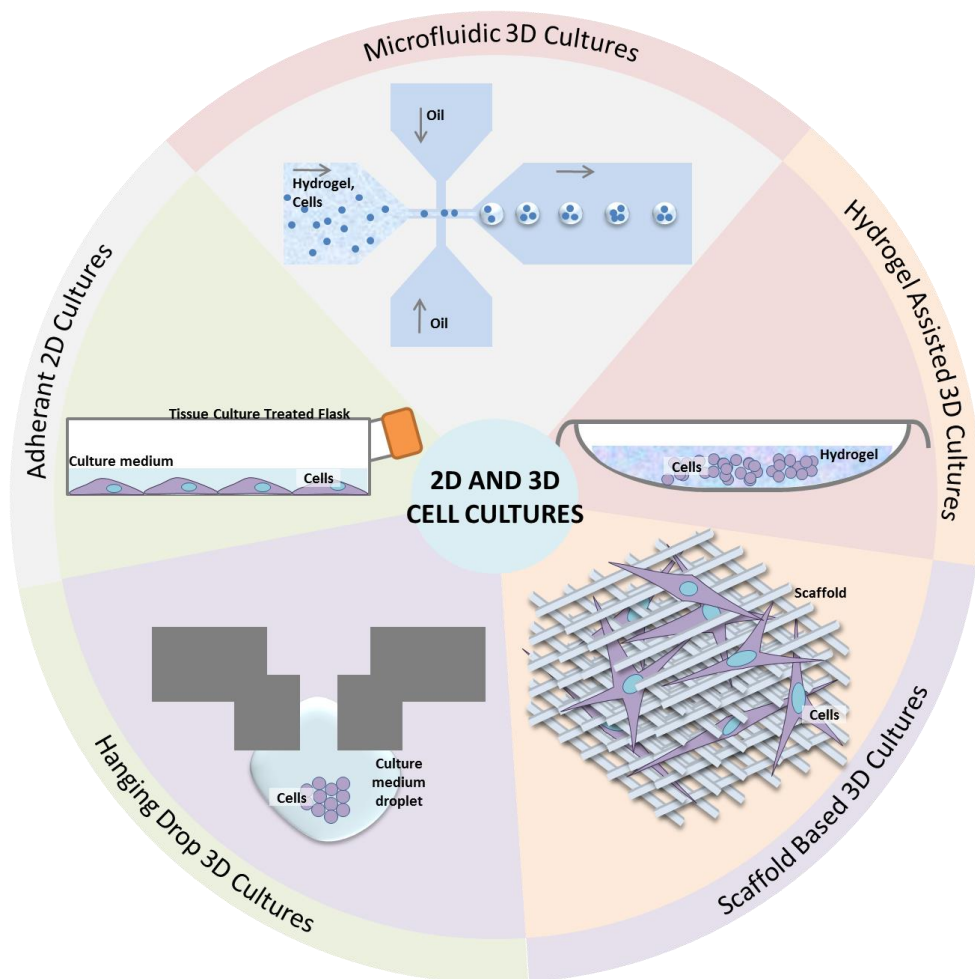


**Figure 5.1** Schematics illustrating 2D and 3D cell culturing techniques.

ECM is the non-cellular component *in vivo*, surrounding and physically supporting the cells and tissues. It is agreed that ECM participates in, and often initiates biochemical and biophysical signals in most biological processes including cellular differentiation, embryogenesis and morphogenetic events (79). An intuitively obvious need for 3D cell cultures in research can be rhetoric – if the cells *in vivo* have extracellular polymers and neighbors in 3D, why not the cells in

research? It would be reasonable to speculate that the contemporary imaging techniques were limited to visualize and observe the cellular processes real time only for 2D cultures. Further, introduction of 3D cultures, and hence ECM *in vitro* had to be preceded by improvements in purification and analytical sciences.

Before proceeding, it might be useful to throw light on cell culturing *in vitro*. Mammalian cells, *in vivo*, can be visualized to be growing in *solid chunks* – in physical contact with the neighboring cells and the ECM – as is typical for most cells in the epithelial, muscle, nervous and solid connective tissue. Some other cells can also be found floating in a liquid medium – for instance, the cells of hematopoietic lineage commonly in the blood and the lymph. It is important to stress the need of contact, *i.e.* the biomechanical cues required for cell proliferation, which is also evident from *in vitro* culturing practices. Most of the established cell lines, and primary cells cultured *in vitro*, are grown in adherent cell cultures. In a typical adherent cell culture, a suspension of cells in a nutrient rich, suitably supplemented culture medium is seeded into ‘tissue culture treated’ polystyrene culture dishes. The surface is essentially rendered hydrophilic or charged, to promote the adhesion proteins, found in abundance in the serum (a component of the culture medium), to mediate adhesion of the cells to the surface. Alternatively, the surface of the culture dish might bear a layer of pre-polymerized ECM. This is a typical 2D cell culture, *i.e.* only a monolayer of cells grows attaching to the plastic surface – at least at low enough cell densities, see Figure 5.1. An important piece of this puzzle is the serum, which is essential as it provides adhesion proteins for the cells to adhere on the substrate and proliferate.

A 3D cell culture, on the other hand, is not grown in a monolayer, and may or may not comprise of a scaffold, as illustrated in Figure 5.1. A hanging drop culture is the simplest example of a 3D culture, in which the cells are grown in a three-dimensional proximity, but are scaffold-free, yet forming a spheroid (80). The method is relatively easy to implement, and includes multi-polarized inter-cellular

interactions, but lacks the biomechanical cues, crucial for several biological processes (81). In a typical hydrogel assisted 3D cell culture, the cells are added to the nutrient medium containing a precursor for a hydrogel, which polymerizes or swells by additional chemical or thermal curing. This hydrogel acts as the ECM *in vivo*, and supports cell proliferation. Such 3D cultures can be grown in dishes or as spheroids, and are the most holistic in terms of replicating the microenvironment *in vivo* (81). Further, mammalian cells can also be 3D cultured on polymeric or ceramic scaffolds, on micro-patterned surfaces, and as hydrogel assisted spheroids on microfluidic platforms. The latter is described in greater details in the following section.

## MICROFLUIDICS AND 3D CELL CULTURE

Although functioning methods exist, microscopic imaging of 3D cell cultures can be daunting. While confocal microscopy offers a penetration depth of only up to 100  $\mu\text{m}$ , it is possible to resort to techniques like multiphoton microscopy and optical coherence tomography (82). Further, there is a loss of degree in the control of microenvironment in these techniques due to reliance on bulk volumetric mass transfer for gas, metabolite and nutrient diffusion to and from the cells. The heterogeneity in bulk polymerization may result in scaffolds or hydrogels that are not uniform. Also, the seeding density of the cells can be difficult to control and reproduce. In addition, spheroids between 200  $\mu\text{m}$  and 500  $\mu\text{m}$  in diameters are known to exhibit radial chemical gradients, while larger spheroids also may undergo central secondary necrosis (83). These lacunae opened the doors of 3D cell culturing and analysis to microfluidic technology (84).

Microfluidics has been exploited to synthesize highly controlled and versatile microfibers for tissue culture in various hydrogel materials. In 2007, Shin *et al.* reported synthesis of alginate microfibers in alginate with embedded fibroblast cells using coaxial flow systems (85). Hwang *et al.* demonstrated microfluidic fabrication of poly(D,L-lactic-co-glycolic acid) (PLGA) microfibers of controlled

diameters in a coaxial flow wet spinning system, and showed alignment of fibroblast cells on the microfiber as scaffolds (86). Photopolymerization coupled to coaxial flow systems has also been used to synthesize microfibers and micrometer scale tubular structures (87).

Further, microfluidic technologies have been exploited to encapsulate and analyze cells in microgels, as a microfluidic version of the hydrogel assisted 3D cultures. Owing to a significantly higher degree of precision in synthesis and assembly of material in microfluidics, it is possible to create uniform and reproducible microgels encapsulating cells. Moreover, owing to small dimensions of the microgels, microscopic imaging is significantly easier compared to conventional hydrogel assisted 3D culturing, using widely available epifluorescent and confocal microscopes in research labs. Microcluster-spheroids of different cell types have been cultured and studied in microwell formats or by microimprinting (88-91). Aung *et al.* used photolithography to create 3D cultures by encapsulating cardiomyocytes in gelatin-methacryloyl and studied the contractile stress upon exposure to epinephrine (92). Another approach to obtain fibroblast-laden hydrogel particles was reported by Panda *et al.* using stop flow lithography (93). It is important to note that, due to requirement of high concentrations of often toxic photoinitiator molecules and high exposure doses of ultraviolet radiation, photopolymerization is usually not preferred for encapsulating cells in hydrogels.

It is interesting to note that the major player in this field remains droplet microfluidics, wherein the aqueous phase, containing the cell suspensions and hydrogel precursor, is dispersed in a continuous oil phase (94). One of the first reports to encapsulate cells in hydrogel droplets in microfluidics was published in 2007 by Tan *et al.* wherein they used a T-junction to create calcium alginate microbeads containing cells of T-lymphocytic origin (95). In 2013, Ma *et al.* reported hybrid collagen and gelatin microbeads with encapsulated cells of fibroblast origin, and demonstrated the potential to maintain them in culture for a

week (96). In last decade, several works have exploited this technology to study biological problems requiring 3D cell cultures. Wang *et al.* established an anti-cancer drug testing model with human cervical carcinoma cells in mixed alginate and matrigel microbeads, based on cell viability (97). In a similar work, Sabhachandani *et al.* studied dose response of doxorubicin and doxorubicin-paclitaxel on cell viability in cell-laden alginate microbeads for single cell type, as well as co-cultures (98). A recent work by Jang *et al.* reported the interactions of two different gastric cancer cell lines with the ECM by encapsulating cells in collagen microgels, and established a model for the progression of cancer via epithelial mesenchymal transition and drug resistance.

## ECM AND CANCER

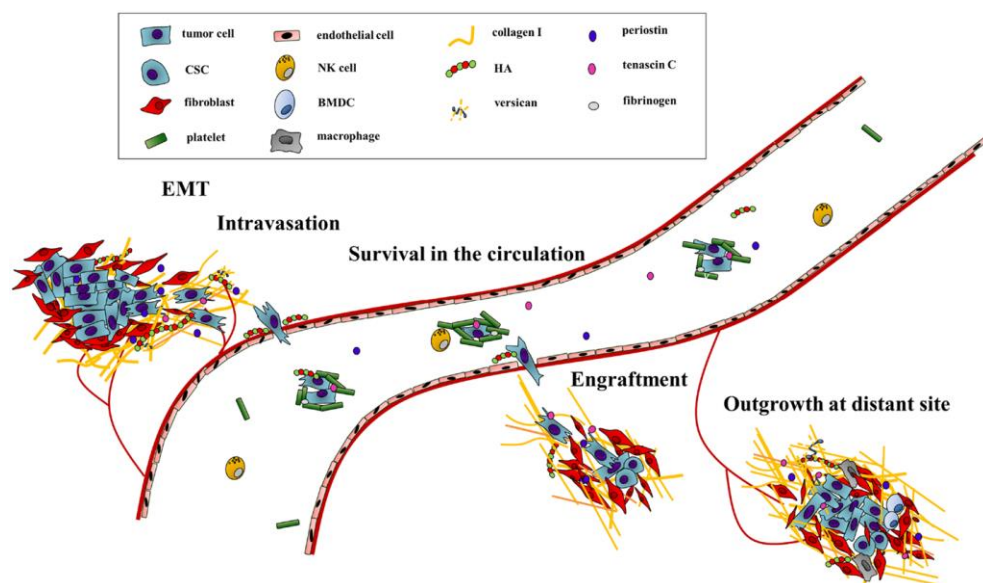


**Figure 5.2** The interplay of extra-cellular matrix and cancer development. Graphics reproduced from reference (99) by permissions under Creative Commons Attribution License (CC BY).

It is curious to note that a significant proportion of the studies involving microgel and 3D cell cultures focus on cancer development, progression and drug resistance. While ECM is a crucial participant in general tissue homeostasis, the underlying conduit of this directed research is attributed to the importance and involvement of ECM in tumor progression. ECM is known to partake in growth of tumors by providing pro-proliferation cues and impeding apoptotic stimuli. It also plays a key role in dissemination of tumor cells during metastasis. Additionally, the collagen fibers of ECM can act as a barrier for efficient drug delivery (99, 100). An in-depth discussion of the role of ECM is beyond the scope of this thesis. However, Figure 5.2 highlights the important stages at which the ECM is involved in cancer and tumor development.

The last decade has seen significant amount of effort being invested into drug discovery for targeting ECM or ECM modifications (99). The trend is reinforced by the previously mentioned research into 3D culture models of cancer cells and tissues. Unsurprisingly, the mechanical properties of the ECM are altered during the progress of cancer, in order to facilitate metastasis. Further, there is new interest in research regarding cell fate dependence on the mechanical properties of the ECM, especially for breast cancer (101). A new approach to study this is to mechanically characterize bulk 3D hydrogel-cancer cell cultures (102). In this chapter, we are building towards the study of micrometer ranged 3D cultures of cells of breast cancer origin in collagen microgels. For this purpose, we aim to exploit droplet microfluidics and deformability-coupled DLD to study and fractionate cell-laden microgels into subpopulations to provide a semi-quantitative model for mechanical characterization in a label-free manner. Before proceeding, the next section gives a brief overview of the principle of droplet microfluidics.

## DROPLET MICROFLUIDICS

Droplet microfluidics exploits the principle of microfluidics and emulsion sciences to produce highly controlled and uniform droplets in the range of submicrometers

to several hundred micrometers. The technology has been exploited to produce oil in water (o/w) as well as water in oil (w/o) droplets. Essentially, droplets provide an elegant way of performing reactions in closed reservoirs of picoliter volumes.

Droplet formation and stabilization is a function of the physical forces at the interface of the two fluids. In an emulsion, as one of the fluids is hydrophilic and the other hydrophobic, there exists an interfacial tension,  $\gamma$  at the boundary of the two, which in turn gives rise to a surface energy. It is possible to estimate **Laplace pressure** between the inside and outside of a droplet with the two major radii of curvature  $R_1$  and  $R_2$  as equation 5.1.

$$\Delta P = \gamma \left( \frac{1}{R_1} + \frac{1}{R_2} \right) \quad 5.1$$

To obtain a stable interface between the two fluids, the pressure across the interface needs to be minimized, for which, it is possible to show that  $R_1 = R_2$ . Hence, this is intrinsically achieved by the droplet by attaining a spherical shape. Analogously, in order to minimize the free energy of the system, and hence, the surface energy of the droplet, the surface area needs to be minimized – as in case of a sphere.

Further, as the droplets are in flow, with velocity  $U$ , the other dominant physical parameter of the system is the characteristic viscosity,  $\eta$ . These parameters are in constant competition and the balance determines the stability of the droplets. While the dominant viscosity of the system acts to deform a droplet, the interfacial tension works to keep the surface intact and unpierced. This balance is represented by the dimensionless quantity, **Capillary number**  $Ca$ .

$$Ca = \frac{\eta U}{\gamma} \quad 5.1$$

For high  $Ca$ , viscous forces dominate to deform the droplets, while for low  $Ca$ , interfacial tension maintains the droplets spherical. Further, due to high surface area to volume ratios at this scale, the surface energy per droplet can be significantly high, which in turn might lead to droplet coalescence. For stabilization of the droplet, it is crucial to use amphiphilic molecules, *i.e.* **surfactants**, that act to reduce the interfacial energy of the system (103). Also, the surface chemistry of the **channel walls** is crucial for droplet stability and generation. For w/o droplets, hydrophobic channels are desirable, while o/w droplets call for hydrophilic channels.

Broadly, **droplet generation** can be classified into active or passive methods (104). The former uses external actuation forces to enable droplet formation, including electrical, magnetic, centrifugal, thermal, optical and mechanical forces; while the latter relies on fluid instabilities in a two phase flow. Each method has its own pros and cons. However, the current work focuses on the passive droplet generation for reasons including economical droplet production and device fabrication. Passive droplet generators can also be further divided into three major classes based on device design – co-flow, cross-flow (T-junctions) and flow-focusing generators, see Figure 5.3. Essentially, the external flow and viscous shear stresses compete against the capillary pressure across the interface at the neck, thereby determining the size of the droplet. **Co-flow** droplet generators comprise of a multi-planar device, usually assembled by integrating capillaries of different sizes. The fluid in the internal capillary is the dispersed phase, while the annular fluid becomes the continuous phase. Droplet pinch off can occur in two different regimes known as dripping and jetting (103). Dripping regime is characterized by droplet nicking near the mouth of the capillary. As the velocity of the continuous phase is increased, the dispersed phase forms a thread, and the droplet nicking takes place downstream. Although co-flow droplet generators are

versatile and facilitate reproducible droplet generation, the non-planar geometry renders them difficult to manufacture.

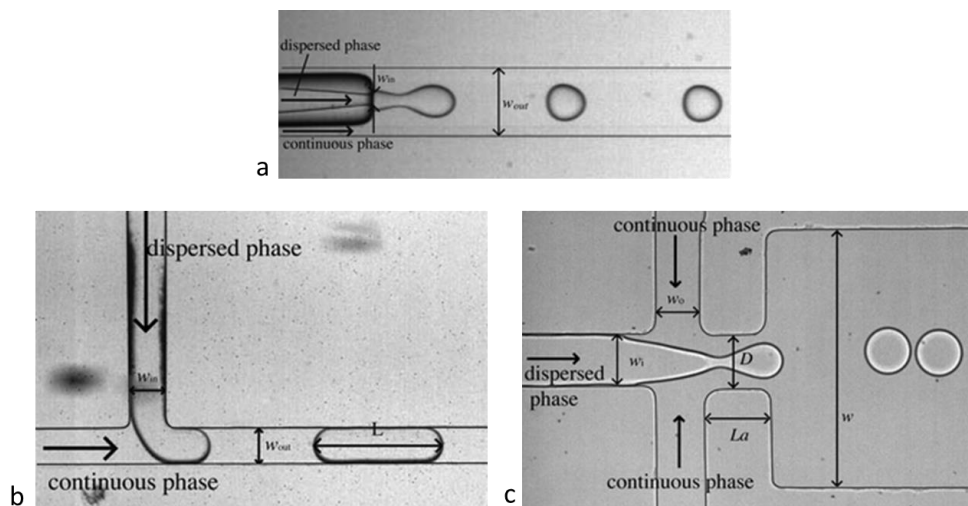


**Figure 5.3** Common methods of passive droplet generation. a) Co-flow, b) Cross-flow, and c) Focused-flow droplet generators. Reused from reference (103) with permission from the Royal Society of Chemistry.

In a **cross-flow** droplet generator, the dispersed phase meets the continuous phase at an angle, usually orthogonally. For  $w_{in} \ll w_{out}$  (see Figure 5.3 b), and large  $Ca$ , when the viscous shear stress overcomes the interfacial tension, the droplets break off (103). This is known as dripping regime, wherein the droplets are nicked before blocking the main channel. For  $w_{in} \approx w_{out}$  and low  $Ca$ , the dispersed phase enters and restricts flow of the continuous phase in the main channel, thereby leading to a sudden increase in the pressure upstream. Consequently, the droplet is nicked in a fashion called the squeezing regime. If the flow velocity of the dispersed phase is higher than that of the continuous phase, a stable co-flow of the two fluids may exist. Although simple to manufacture, reproducibility and size variation in cross-flow droplet generators remains a major issue.

Of particular interest are **flow-focused** droplet generators. Highly versatile, they provide significantly higher generation frequencies of droplets – up to a 100 kHz. As evident in Figure 5.3 c, the large number of geometrical parameters render droplet scaling laws in such devices indeterminable. However, squeezing, dripping, jetting and thread formation regimes are known to exist in flow-focused droplet generators (103). In the following sections, we present preliminary results for fabricating w/o droplets in flow-focused geometries, and the future work towards establishing a label-free cancer cell-ECM interaction and sorting microfluidic platform.

## 5.2 RESULTS AND DISCUSSIONS

### POLYACRYLAMIDE DROPLETS

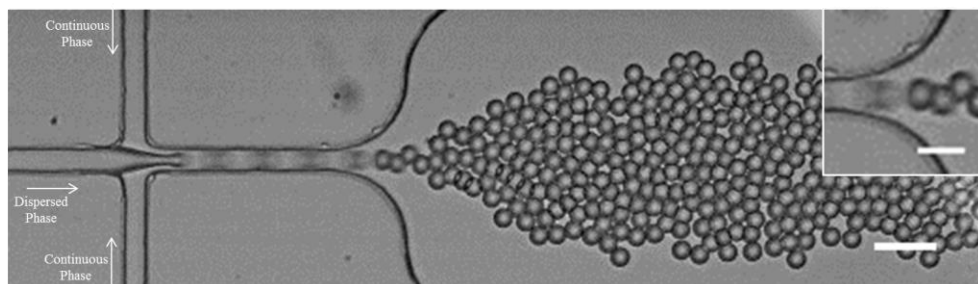


**Figure 5.4** Generation of 11  $\mu\text{m}$  polyacrylamide microbeads in a focused-flow device at 10X magnification (scale bar 50  $\mu\text{m}$ ). Inset shows a zoomed in image at the point of generation (scale bar 25  $\mu\text{m}$ ). Average diameter of droplets was measured to be  $12.7 \pm 0.9 \mu\text{m}$ . Dispersed phase is polyacrylamide monomer solution, while continuous phase is HFE-7500 with a custom-synthesized fluorosurfactant.

In order to establish a suitable model for hydrogel droplets, the preliminary work was performed on Polyacrylamide microbeads in a flow-focused droplet generator with a nozzle width of 15  $\mu\text{m}$  (Dev15). Different concentrations of Acrylamide between 0.07% and 0.13% were used to produce droplets in a flow-focused

droplet generator with a nozzle size of 15  $\mu\text{m}$ . The operational pressures of continuous phase and dispersed phase were selected to produce beads of around 11  $\mu\text{m}$  on the chip (see Figure 5.4).

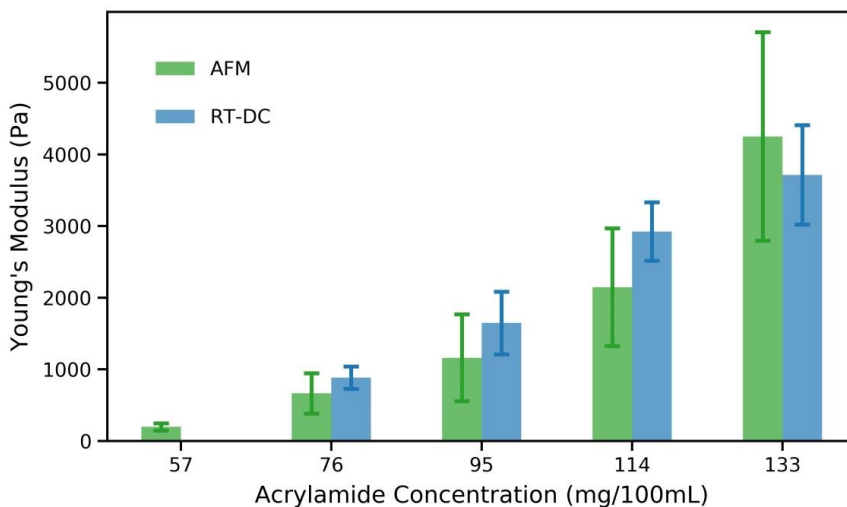


**Figure 5.5** Young's modulus of the polyacrylamide beads, measured using Atomic Force Microscopy (AFM) and Real Time Deformability Cytometry (RT-DC).

The production rate was too fast to visualize individual droplet generation, hence the generation rate was calculated indirectly by accounting volumetric consumption, and was determined to be around 80 – 100 kHz. The high droplet generation rate can be attributed to high operational pressures (around 900 mbar and 800 mbar for continuous phase and dispersed phase, respectively) and the design of the Dev15 (see Figure 5.4), wherein after the point of droplet generation (15  $\mu\text{m}$  width), the hydraulic resistance drastically decreases due to a wide relief region of 250  $\mu\text{m}$ . Further, the droplets were mechanically characterized using Atomic Force Microscopy (AFM) and Real Time Deformability Cytometry (RT-DC) (105). As is evident from Figure 5.5, an increasing acrylamide precursor concentration yielded stiffer droplets.

## COLLAGEN DROPLETS

Polyacrylamide is not suitable for cell encapsulation because of high monomer toxicity, hence we selected Collagen-1 as the dispersed phase. Collagen-1 is the most abundant component of ECM *in vivo*, and is, hence, the substrate of choice for spheroid 3D cultures. For this purpose, Dev15 was used. In order to characterize the system, droplet production was aimed at a frequency of around 20 Hz with the equal operational pressures for the dispersed and continuous phase. However, the generation rate significantly reduced within 20 minutes (see Figure 5.6). Also, the droplet diameter reduced from  $23 \pm 21 \mu\text{m}$  to  $21.7 \pm 1.3 \mu\text{m}$ . This was attributed to rapid polymerization of collagen at room temperature.

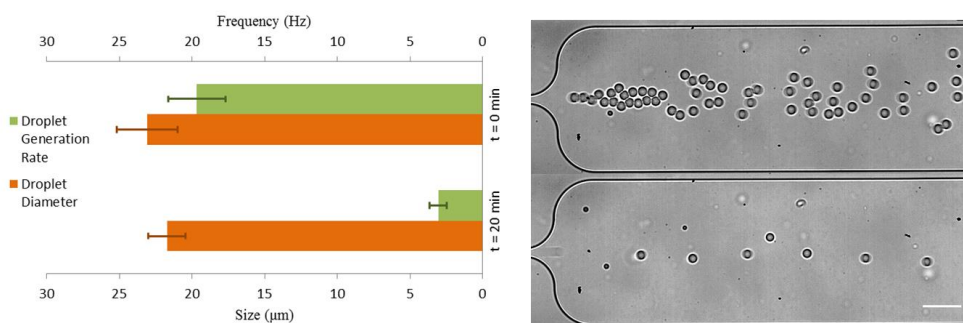


**Figure 5.6** Time evolution of collagen-1 droplets in a flow-focused droplet device. On the left, droplet generation rate and diameters of the collagen droplets at 0 and 20 minutes. On the right, micrographs showing drastic reduction in droplet generation rate; flow is left to right (scale bar 100  $\mu\text{m}$ ).

As the 15  $\mu\text{m}$  nozzle was not suitable to produce large droplets for cell encapsulation, we resorted to a commercial hydrophobic droplet generator with a nozzle size of 75  $\mu\text{m}$  (Dev75), capable of producing droplets above 100  $\mu\text{m}$  in diameter. The device was connected to off-chip reservoirs that could be immersed in ice, in order to prevent thermal gelation of Collagen-1 (see Figure 5.9).

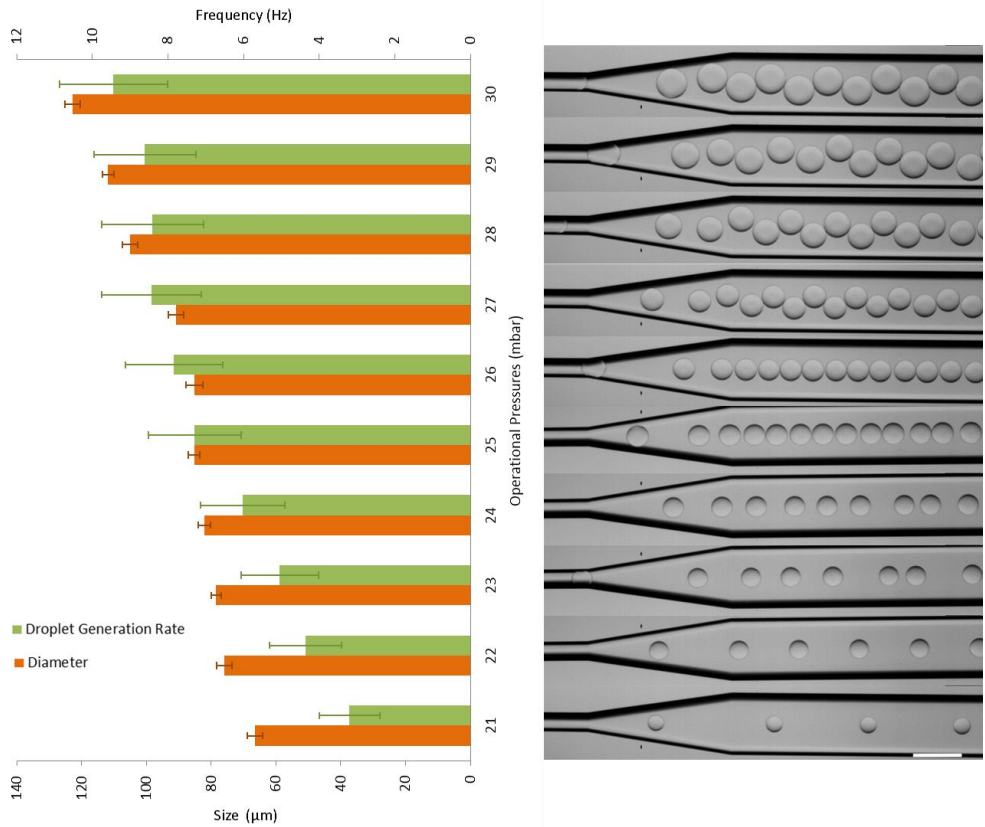


**Figure 5.7** Effect of operational pressure on the droplet diameter and generation rate in Dev75. On the right, micrographs at 10X magnification showing droplet generation at corresponding operating pressures; flow is left to right. Scale bar 200  $\mu\text{m}$ .

We started by calibrating the new setup, due to incorporation of an off-chip reservoir and a device design with significantly lower hydraulic resistance. Droplet generation in Dev75 was carried out first with w/o droplets using distilled water as dispersed phase, and Picosurf-1 (2% in FC-40) as the continuous phase, both immersed in ice. As shown in Figure 5.7, with increasing applied pressure, the diameter of the droplets increased from 66  $\mu\text{m}$  to 123  $\mu\text{m}$ . Also, the frequency of generation increased from 3.2 to 9.2 Hz. However, it was realized that the due to the low hydraulic resistance of the device, vertical positioning of the external

reservoirs also interfered with the driving pressures. As is evident from Figure 5.7, 1 mbar pressure difference – equivalent to 1 cm of hydrostatic pressure – can create significant changes in the regime.

Further, collagen-1 droplets were generated in Dev75 in the setup shown in Figure 5.9, with the off-chip reservoirs immersed in ice. As shown in Figure 5.8, for similar applied operational pressures, the droplets were not stable. As the applied pressure for continuous phase was increased, a stable production of droplets was achieved for 71  $\mu\text{m}$  droplets at 3 Hz. However, due to the magnified effect of vertical positioning of the off-chip reservoirs, the observations were not reproducible at constant operational pressures. Moreover, collagen pre-polymer underwent gelation due to local heating from the illumination.

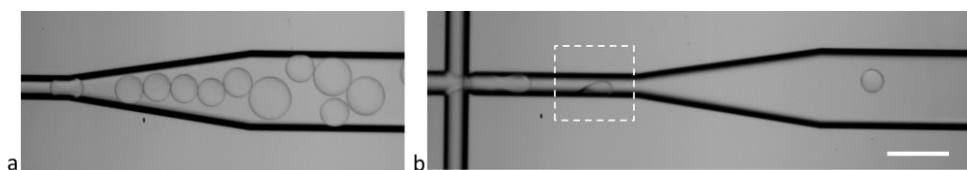


**Figure 5.8** Collagen-1 droplets in Dev75 with continuous phase (Picosurf-1 (2% in FC-40)) and dispersed phase (collagen-1 pre-polymer solution) at 26 mbar and 25 mbar, and b) 38 mbar and 24 mbar. The highlighted area shows gelation of collagen-1 in the device due to local heating from illumination.

### 5.3 FUTURE WORK

The current work has helped to establish collagen-1 based microgel synthesis. Some technical constraints have been identified. The next step would be to establish standard reproducible protocols for production of collagen-1 microgels, following by integration of cell encapsulation using droplet microfluidics. Development of a suitable design for a mesoscopic DLD device is underway.

## 5.4 METHODS

### DEVICE DESIGN AND FABRICATION

The device design for production of 15  $\mu\text{m}$  diameter droplets (Dev15) was kindly shared by our collaborator Salvatore Girardo, Technical University, Dresden, Germany. The photolithography with SU8 and device assembly was performed as described earlier in Section 4.4.

Hydrophobic devices for droplet production of nominal diameter 75  $\mu\text{m}$  (DGFF.75.2), along with the adapter assembly, Fluidic Connect Pro were purchased from Micronit, Enschede, The Netherlands.

### SAMPLE PREPARATION

Polyacrylamide monomer solution was prepared using suitable volumes of aqueous solutions of 40% Acrylamide (Sigma Aldrich, Germany), 2% Bisacrylamide (Sigma Aldrich, Germany), 10% Ammonium persulfate (GE Healthcare, Germany) and 0.2% Riboflavin (Sigma Aldrich, Germany). Collagen pre-polymer solution was prepared using Rat Tail Collagen Type-1 (Sigma Aldrich, Sweden) and the supplied 5X collagen buffer, 10% (v/v) fetal bovine serum (Sigma Aldrich, Sweden) and Dulbecco's Modified Eagle Medium (Sigma Aldrich) for a final collagen concentration of 1.7  $\text{mg}\cdot\text{ml}^{-1}$ . Fluorinated oil HFE-7500 (3M, Germany), along with 0.4% (v/v) Tetramethylethylenediamine and 1.5% (w/w) EA-surfactant was used as the continuous phase. Alternatively, Picosurf (2% in FC-40) (Dolomite, United Kingdom) was used as the continuous phase.

### DEVICE OPERATION

The device was operated under an inverted microscope using a positive pressure pump, as described earlier in Section 4.4. Samples fluids were loaded on to the off-chip reservoirs Fluiwell-4C (Fluigent, France) immersed in ice, connected to

the device using Teflon tubings (Sigma Aldrich). Fluid was pumped by creating an excess overhead pressure in the off-chip reservoirs using a pressure pump, MFCS-4C Pressure controller (Fluigent, Paris, France). The images were captured using an ultrafast camera, Mikrotron Eosens Mini (Mikrotron GmbH, Germany) and using 10X objective lens (Nikon Plan Fluor 10X/0.30).

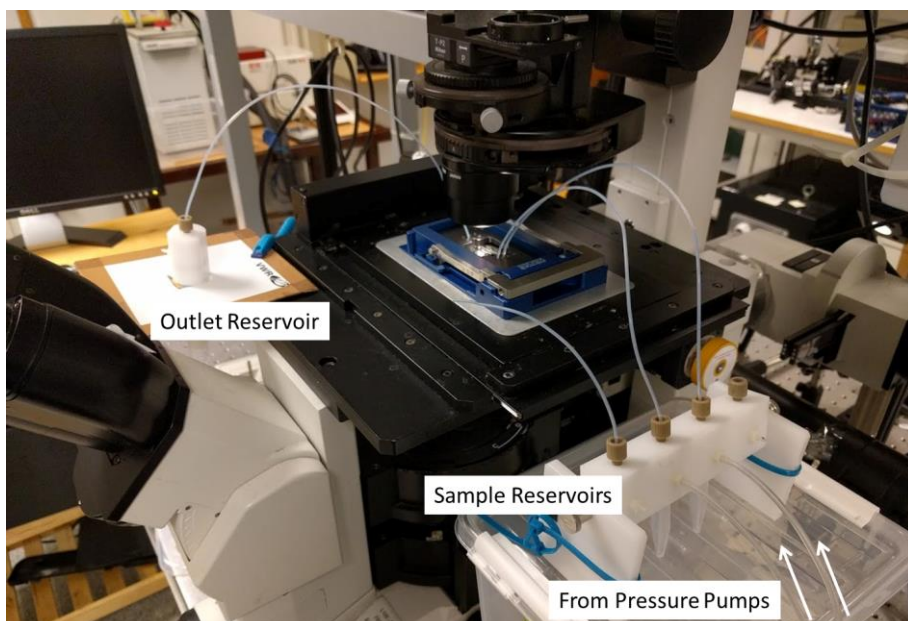


**Figure 5.9** Setup for Collagen-1 droplet generation. The sample reservoirs are connected to a pressure pump, and can be immersed in ice to prevent gelation of Collagen-1.

#### POLYACRYLAMIDE MICROBEADS POLYMERIZATION AND WASHING

Polyacrylamide microbeads were photocured at  $5000 \text{ mJ.cm}^{-2}$  for 10 seconds. The beads were skimmed off by gentle pipetting, and sequentially washed with 20% (v/v) perfluorooctanol (Sigma Aldrich) in of HFE-7500, 1% (v/v) Span-80 (Sigma Aldrich, Germany) and phosphate buffer saline.



## BIBLIOGRAPHY

1. Van Gogh V. Man with Winnow. Otterlo, The Netherlands: Kröller-Müller Museum; 1881.
2. Van Gogh V. Woman Churning Butter. Otterlo, The Netherlands: Kröller-Müller Museum; 1881.
3. Smithies O. Zone electrophoresis in starch gels: group variations in the serum proteins of normal human adults. *Biochemical Journal*. 1955;61(4):629-41.
4. Yalow RS, Glick SM, Roth J, Roth S, Berson SA. Radioimmunoassay of Human Plasma ACTH. *The Journal of Clinical Endocrinology & Metabolism*. 1964;24(11):1219-25.
5. Engvall E, Perlmann P. Enzyme-linked immunosorbent assay (ELISA) quantitative assay of immunoglobulin G. *Immunochemistry*. 1971;8(9):871-4.
6. Van Weemen BK, Schuurs AHWM. Immunoassay using antigen—enzyme conjugates. *FEBS Letters*. 1971;15(3):232-6.
7. Southern EM. Detection of specific sequences among DNA fragments separated by gel electrophoresis. *Journal of Molecular Biology*. 1975;98(3):503-17.
8. Alwine JC, Kemp DJ, Stark GR. Method for detection of specific RNAs in agarose gels by transfer to diazobenzyloxymethyl-paper and hybridization with DNA probes. *Proceedings of the National Academy of Sciences*. 1977;74(12):5350-4.
9. Renart J, Reiser J, Stark GR. Transfer of proteins from gels to diazobenzyloxymethyl-paper and detection with antisera: a method for studying antibody specificity and antigen structure. *Proc Natl Acad Sci U S A*. 1979;76(7):3116-20.

10. Mullis KB. Process for amplifying nucleic acid sequences. US Patent 4,683,202; 1987.
11. Xia Y, Whitesides GM. SOFT LITHOGRAPHY. *Annual Review of Materials Science*. 1998;28(1):153-84.
12. Sajeesh P, Sen AK. Particle separation and sorting in microfluidic devices: a review. *Microfluid Nanofluid*. 2014;17(1):1-52.
13. Brody JP, Osborn TD, Forster FK, Yager P. A planar microfabricated fluid filter. *Sensors and Actuators A: Physical*. 1996;54(1):704-8.
14. Yager P, Brody JP. Absorption-enhanced differential extraction device. *Google Patents*; 1997.
15. Cho BS, Schuster TG, Zhu X, Chang D, Smith GD, Takayama S. Passively Driven Integrated Microfluidic System for Separation of Motile Sperm. *Analytical Chemistry*. 2003;75(7):1671-5.
16. Yamada M, Nakashima M, Seki M. Pinched Flow Fractionation: Continuous Size Separation of Particles Utilizing a Laminar Flow Profile in a Pinched Microchannel. *Analytical Chemistry*. 2004;76(18):5465-71.
17. Takagi J, Yamada M, Yasuda M, Seki M. Continuous particle separation in a microchannel having asymmetrically arranged multiple branches. *Lab on a Chip*. 2005;5(7):778-84.
18. Morijiri T, Sunahiro S, Senaha M, Yamada M, Seki M. Sedimentation pinched-flow fractionation for size- and density-based particle sorting in microchannels. *Microfluid Nanofluid*. 2011;11(1):105-10.
19. Park J-S, Jung H-I. Multiorifice Flow Fractionation: Continuous Size-Based Separation of Microspheres Using a Series of Contraction/Expansion Microchannels. *Analytical Chemistry*. 2009;81(20):8280-8.

20. Yoon DH, Ha JB, Bahk YK, Arakawa T, Shoji S, Go JS. Size-selective separation of micro beads by utilizing secondary flow in a curved rectangular microchannel. *Lab on a Chip*. 2009;9(1):87-90.
21. Ji HM, Samper V, Chen Y, Heng CK, Lim TM, Yobas L. Silicon-based microfilters for whole blood cell separation. *Biomedical Microdevices*. 2008;10(2):251-7.
22. Yamada M, Seki M. Hydrodynamic filtration for on-chip particle concentration and classification utilizing microfluidics. *Lab on a Chip*. 2005;5(11):1233-9.
23. Huang LR, Cox EC, Austin RH, Sturm JC. Continuous Particle Separation Through Deterministic Lateral Displacement. *Science*. 2004;304(5673):987-90.
24. Guo Q, Duffy SP, Matthews K, Islamzada E, Ma H. Deformability based Cell Sorting using Microfluidic Ratchets Enabling Phenotypic Separation of Leukocytes Directly from Whole Blood. *Scientific Reports*. 2017;7(1):6627.
25. Beech JP, Holm SH, Adolfsson K, Tegenfeldt JO. Sorting cells by size, shape and deformability. *Lab on a Chip*. 2012;12(6):1048-51.
26. Vesperini D, Chaput O, Munier N, Maire P, Edwards-Lévy F, Salsac A-V, et al. Deformability- and size-based microcapsule sorting. *Medical Engineering & Physics*. 2017;48(Supplement C):68-74.
27. Mohamed H, Murray M, Turner JN, Caggana M. Isolation of tumor cells using size and deformation. *Journal of Chromatography A*. 2009;1216(47):8289-95.
28. Hou HW, Bhagat AAS, Lin Chong AG, Mao P, Wei Tan KS, Han J, et al. Deformability based cell margination-A simple microfluidic design for malaria-infected erythrocyte separation. *Lab on a Chip*. 2010;10(19):2605-13.

29. Dahm R. Friedrich Miescher and the discovery of DNA. *Developmental Biology*. 2005;278(2):274-88.
30. De Laval G. Centrifugal separator. Google Patents; 1881.
31. B NJ, Svedberg T. Analytical centrifuge. Google Patents; 1927.
32. Jens D, Stefan H, Sascha L, Sarah P, Felix von S, Roland Z. The centrifugal microfluidic Bio-Disk platform. *Journal of Micromechanics and Microengineering*. 2007;17(7):S103.
33. Park J, Sunkara V, Kim T-H, Hwang H, Cho Y-K. Lab-on-a-Disc for Fully Integrated Multiplex Immunoassays. *Analytical Chemistry*. 2012;84(5):2133-40.
34. Ukita Y, Oguro T, Takamura Y. Density-gradient-assisted centrifugal microfluidics: an approach to continuous-mode particle separation. *Biomedical microdevices*. 2017;19(2):24.
35. Sun Y, Sethu P. Microfluidic Adaptation of Density-Gradient Centrifugation for Isolation of Particles and Cells. *Bioengineering*. 2017;4(3):67.
36. Haerberle S, Brenner T, Zengerle R, Ducree J. Centrifugal extraction of plasma from whole blood on a rotating disk. *Lab on a Chip*. 2006;6(6):776-81.
37. Moen ST, Hatcher CL, Singh AK. A Centrifugal Microfluidic Platform That Separates Whole Blood Samples into Multiple Removable Fractions Due to Several Discrete but Continuous Density Gradient Sections. *PLOS ONE*. 2016;11(4):e0153137.
38. Riegger L, Grumann M, Steigert J, Lutz S, Steinert C, Mueller C, et al. Single-step centrifugal hematocrit determination on a 10- $\mu$  processing device. *Biomedical microdevices*. 2007;9(6):795-9.
39. Henderson B, Kinahan DJ, Ducreé J. The Centrifugal Microfluidic: Lab-on-a-Disc Platform. In: Dixit CK, Kaushik A, editors. *Microfluidics for Biologists*:

Fundamentals and Applications. Cham: Springer International Publishing; 2016. p. 115-44.

40. Benincasa M-A, Moore LR, Williams PS, Poptic E, Carpino F, Zborowski M. Cell Sorting by One Gravity SPLITT Fractionation. *Analytical Chemistry*. 2005;77(16):5294-301.

41. Huh D, Bahng JH, Ling Y, Wei H-H, Kripfgans OD, Fowlkes JB, et al. Gravity-driven microfluidic particle sorting device with hydrodynamic separation amplification. *Analytical chemistry*. 2007;79(4):1369-76.

42. Sugiyama D, Teshima Y, Yamanaka K, Briones-Nagata MP, Maeki M, Yamashita K, et al. Simple density-based particle separation in a microfluidic chip. *Analytical Methods*. 2014;6(1):308-11.

43. Son JH, Lee SH, Hong S, Park S-m, Lee J, Dickey AM, et al. Hemolysis-free blood plasma separation. *Lab on a Chip*. 2014;14(13):2287-92.

44. Holm SH, Beech JP, Tegenfeldt JO. Density-based particle fractionation. 18th International Conference on Miniaturized Systems for Chemistry and Life Sciences; October 26-30, 2014; San Antonio, Texas, USA: The Royal Society of Chemistry; 2014.

45. Maria MS, Rakesh PE, Chandra TS, Sen AK. Capillary flow-driven microfluidic device with wettability gradient and sedimentation effects for blood plasma separation. *Scientific Reports*. 2017;7:43457.

46. Holm SH, Beech JP, Barrett MP, Tegenfeldt JO. Separation of parasites from human blood using deterministic lateral displacement. *Lab Chip*. 2011;11(7):1326-32.

47. Sugaya S, Yamada M, Seki M. Observation of nonspherical particle behaviors for continuous shape-based separation using hydrodynamic filtration. *Biomicrofluidics*. 2011;5(2):024103.

48. Masaeli M, Sollier E, Amini H, Mao W, Camacho K, Doshi N, et al. Continuous inertial focusing and separation of particles by shape. *Physical Review X*. 2012;2(3):031017.
49. Davis JA. *Microfluidic Separation of Blood Components Through Deterministic Lateral Displacement*: Princeton University; 2008.
50. Domínguez M, Moreno I, Aizpurua C, Toraño A. Early mechanisms of Leishmania infection in human blood. *Microbes and Infection*. 2003;5(6):507-13.
51. Bailey F, Mondragon-Shem K, Hotez P, Ruiz-Postigo JA, Al-Salem W, Acosta-Serrano A, et al. A new perspective on cutaneous leishmaniasis—Implications for global prevalence and burden of disease estimates. *PLoS Negl Trop Dis*. 2017;11(8):e0005739.
52. Barrett MP, Croft SL. Management of trypanosomiasis and leishmaniasis. *British Medical Bulletin*. 2012;104(1):175-96.
53. Croft SL, Olliaro P. Leishmaniasis chemotherapy—challenges and opportunities. *Clinical Microbiology and Infection*. 2011;17(10):1478-83.
54. Dominguez M, Moreno I, Aizpurua C, Torano A. Early mechanisms of Leishmania infection in human blood. *Microbes Infect*. 2003;5(6):507-13.
55. Daboul MW. Promastigote Existence in Infected Lesions of Cutaneous Leishmaniasis. *Journal of General Practice*. 2014.
56. Wheeler RJ, Gluenz E, Gull K. The cell cycle of Leishmania: morphogenetic events and their implications for parasite biology. *Molecular Microbiology*. 2011;79(3):647-62.
57. Inglis DW. Efficient microfluidic particle separation arrays. *Applied Physics Letters*. 2009;94(1):013510.
58. McGrath J, Jimenez M, Bridle H. Deterministic lateral displacement for particle separation: a review. *Lab on a Chip*. 2014;14(21):4139-58.

59. Loutharback K, Puchalla J, Austin RH, Sturm JC. Deterministic microfluidic ratchet. *Physical review letters*. 2009;102(4):045301.
60. Loutharback K, Chou KS, Newman J, Puchalla J, Austin RH, Sturm JC. Improved performance of deterministic lateral displacement arrays with triangular posts. *Microfluid Nanofluid*. 2010;9(6):1143-9.
61. Loutharback K, D'Silva J, Liu L, Wu A, Austin RH, Sturm JC. Deterministic separation of cancer cells from blood at 10 mL/min. *AIP Advances*. 2012;2(4):042107.
62. Liu Z, Huang F, Du J, Shu W, Feng H, Xu X, et al. Rapid isolation of cancer cells using microfluidic deterministic lateral displacement structure. *Biomicrofluidics*. 2013;7(1):011801.
63. Al-Fandi M, Al-Rousan M, Jaradat MAK, Al-Ebbini L. New design for the separation of microorganisms using microfluidic deterministic lateral displacement. *Robotics and Computer-Integrated Manufacturing*. 2011;27(2):237-44.
64. Zeming KK, Ranjan S, Zhang Y. Rotational separation of non-spherical bioparticles using I-shaped pillar arrays in a microfluidic device. *Nature Communications*. 2013;4:1625.
65. Hyun J-c, Hyun J, Wang S, Yang S. Improved pillar shape for deterministic lateral displacement separation method to maintain separation efficiency over a long period of time. *Separation and Purification Technology*. 2017;172:258-67.
66. Zhang Z, Henry E, Gompper G, Fedosov DA. Behavior of rigid and deformable particles in deterministic lateral displacement devices with different post shapes. *The Journal of chemical physics*. 2015;143(24):243145.

67. Kulrattanarak T, van der Sman RGM, Schroën CGPH, Boom RM. Analysis of mixed motion in deterministic ratchets via experiment and particle simulation. *Microfluid Nanofluid.* 2011;10(4):843-53.
68. Wichterle O, Lim D. Hydrophilic Gels for Biological Use. *Nature.* 1960;185(4706):117-8.
69. Lee SC, Kwon IK, Park K. Hydrogels for Delivery of Bioactive Agents: A Historical Perspective. *Advanced drug delivery reviews.* 2013;65(1):17-20.
70. Yarimitsu S, Sasaki S, Murakami T, Suzuki A. Evaluation of lubrication properties of hydrogel artificial cartilage materials for joint prosthesis. *Biosurface and Biotribology.* 2016;2(1):40-7.
71. Sikareepaisan P, Ruktanonchai U, Supaphol P. Preparation and characterization of asiaticoside-loaded alginate films and their potential for use as effectual wound dressings. *Carbohydrate Polymers.* 2011;83(4):1457-69.
72. El-Sherbiny IM, Yacoub MH. Hydrogel scaffolds for tissue engineering: Progress and challenges. *Global Cardiology Science & Practice.* 2013;2013(3):316-42.
73. Antoine EE, Vlachos PP, Rylander MN. Review of Collagen I Hydrogels for Bioengineered Tissue Microenvironments: Characterization of Mechanics, Structure, and Transport. *Tissue Engineering Part B, Reviews.* 2014;20(6):683-96.
74. Parmegiani L, Cognigni GE, Ciampaglia W, Pocognoli P, Marchi F, Filicori M. Efficiency of hyaluronic acid (HA) sperm selection. *Journal of Assisted Reproduction and Genetics.* 2010;27(1):13-6.
75. Tibbitt MW, Anseth KS. Hydrogels as Extracellular Matrix Mimics for 3D Cell Culture. *Biotechnology and bioengineering.* 2009;103(4):655-63.
76. Geckil H, Xu F, Zhang X, Moon S, Demirci U. Engineering hydrogels as extracellular matrix mimics. *Nanomedicine (London, England).* 2010;5(3):469-84.

77. González-Díaz EC, Varghese S. Hydrogels as Extracellular Matrix Analogs. *Gels*. 2016;2(3):20.
78. Ravi M, Paramesh V, Kaviya SR, Anuradha E, Solomon FDP. 3D Cell Culture Systems: Advantages and Applications. *Journal of Cellular Physiology*. 2015;230(1):16-26.
79. Frantz C, Stewart KM, Weaver VM. The extracellular matrix at a glance. *Journal of Cell Science*. 2010;123(24):4195-200.
80. Shri M, Agrawal H, Rani P, Singh D, Onteru SK. Hanging Drop, A Best Three-Dimensional (3D) Culture Method for Primary Buffalo and Sheep Hepatocytes. *Scientific Reports*. 2017;7:1203.
81. Haycock JW. 3D Cell Culture: A Review of Current Approaches and Techniques. In: Haycock JW, editor. *3D Cell Culture: Methods and Protocols*. Totowa, NJ: Humana Press; 2011. p. 1-15.
82. Graf BW, Boppart SA. Imaging and Analysis of Three-Dimensional Cell Culture Models. *Methods in molecular biology (Clifton, NJ)*. 2010;591:211-27.
83. Hirschhaeuser F, Menne H, Dittfeld C, West J, Mueller-Klieser W, Kunz-Schughart LA. Multicellular tumor spheroids: An underestimated tool is catching up again. *Journal of Biotechnology*. 2010;148(1):3-15.
84. Chung BG, Lee K-H, Khademhosseini A, Lee S-H. Microfluidic fabrication of microengineered hydrogels and their application in tissue engineering. *Lab on a Chip*. 2012;12(1):45-59.
85. Shin S-J, Park J-Y, Lee J-Y, Park H, Park Y-D, Lee K-B, et al. "On the Fly" Continuous Generation of Alginate Fibers Using a Microfluidic Device. *Langmuir*. 2007;23(17):9104-8.

86. Hwang CM, Park Y, Park JY, Lee K, Sun K, Khademhosseini A, et al. Controlled cellular orientation on PLGA microfibers with defined diameters. *Biomedical Microdevices*. 2009;11(4):739-46.
87. Jeong W, Kim J, Kim S, Lee S, Mensing G, Beebe DJ. Hydrodynamic microfabrication via "on the fly" photopolymerization of microscale fibers and tubes. *Lab on a Chip*. 2004;4(6):576-80.
88. Kim T, Doh I, Cho Y-H. On-chip three-dimensional tumor spheroid formation and pump-less perfusion culture using gravity-driven cell aggregation and balanced droplet dispensing. *Biomicrofluidics*. 2012;6(3):034107.
89. Lee S-A, No DY, Kang E, Ju J, Kim D-S, Lee S-H. Spheroid-based three-dimensional liver-on-a-chip to investigate hepatocyte-hepatic stellate cell interactions and flow effects. *Lab on a Chip*. 2013;13(18):3529-37.
90. Kim C, Bang JH, Kim YE, Lee SH, Kang JY. On-chip anticancer drug test of regular tumor spheroids formed in microwells by a distributive microchannel network. *Lab on a Chip*. 2012;12(20):4135-42.
91. Kwapiszewska K, Michalczyk A, Rybka M, Kwapiszewski R, Brzozka Z. A microfluidic-based platform for tumour spheroid culture, monitoring and drug screening. *Lab on a Chip*. 2014;14(12):2096-104.
92. Aung A, Bhullar IS, Theprungsirikul J, Davey SK, Lim HL, Chiu Y-J, et al. 3D cardiac [small mu ]tissues within a microfluidic device with real-time contractile stress readout. *Lab on a Chip*. 2016;16(1):153-62.
93. Panda P, Ali S, Lo E, Chung BG, Hatton TA, Khademhosseini A, et al. Stop-flow lithography to generate cell-laden microgel particles. *Lab on a Chip*. 2008;8(7):1056-61.

94. Rossow T, Lienemann PS, Mooney DJ. Cell Microencapsulation by Droplet Microfluidic Templating. *Macromolecular Chemistry and Physics*. 2017;218(2):1600380-n/a.
95. Tan WH, Takeuchi S. Monodisperse Alginate Hydrogel Microbeads for Cell Encapsulation. *Advanced Materials*. 2007;19(18):2696-701.
96. Ma S, Natoli M, Liu X, Neubauer MP, Watt FM, Fery A, et al. Monodisperse collagen-gelatin beads as potential platforms for 3D cell culturing. *Journal of Materials Chemistry B*. 2013;1(38):5128-36.
97. Wang Y, Wang J. Mixed hydrogel bead-based tumor spheroid formation and anticancer drug testing. *Analyst*. 2014;139(10):2449-58.
98. Sabhachandani P, Motwani V, Cohen N, Sarkar S, Torchilin V, Konry T. Generation and functional assessment of 3D multicellular spheroids in droplet based microfluidics platform. *Lab on a Chip*. 2016;16(3):497-505.
99. Venning FA, Wullkopf L, Erler JT. Targeting ECM Disrupts Cancer Progression. *Frontiers in Oncology*. 2015;5:224.
100. Sangaletti S, Chiodoni C, Tripodo C, Colombo MP. The good and bad of targeting cancer-associated extracellular matrix. *Current Opinion in Pharmacology*. 2017;35:75-82.
101. Lee JY, Chaudhuri O. Regulation of Breast Cancer Progression by Extracellular Matrix Mechanics: Insights from 3D Culture Models. *ACS Biomaterials Science & Engineering*. 2018;4(2):302-13.
102. Cox TR, Madsen CD. Relative Stiffness Measurements of Cell-embedded Hydrogels by Shear Rheology in vitro. *EMBO Reports*. 2015.
103. Baroud CN, Gallaire F, Danga R. Dynamics of microfluidic droplets. *Lab on a Chip*. 2010;10(16):2032-45.

104. Zhu P, Wang L. Passive and active droplet generation with microfluidics: a review. *Lab on a Chip*. 2017;17(1):34-75.
105. Otto O, Rosendahl P, Mietke A, Golfier S, Herold C, Klaue D, et al. Real-time deformability cytometry: on-the-fly cell mechanical phenotyping. *Nature methods*. 2015;12(3):199.